

## RESEARCH ARTICLE

10.1002/2016JD025265

## Key Points:

- Modeled photochemical O<sub>3</sub> production is NO<sub>x</sub>-sensitive at a central location in the Colorado Northern Front Range
- Oil and natural gas VOC emissions contribute over 80% to the observed carbon mixing ratio and 17.4% to maximum modeled photochemical O<sub>3</sub>
- Observed O<sub>3</sub> production efficiencies are variable but show an influence of less than 1.8 ppbv/ppbv from oil and natural gas VOC emissions

## Supporting Information:

- Supporting Information S1

## Correspondence to:

S. S. Brown,  
steven.s.brown@noaa.gov

## Citation:

McDuffie, E. E., et al. (2016), Influence of oil and gas emissions on summertime ozone in the Colorado Northern Front Range, *J. Geophys. Res. Atmos.*, 121, 8712–8729, doi:10.1002/2016JD025265.

Received 22 APR 2016

Accepted 5 JUL 2016

Accepted article online 9 JUL 2016

Published online 23 JUL 2016

## Influence of oil and gas emissions on summertime ozone in the Colorado Northern Front Range

Erin E. McDuffie<sup>1,2,3</sup>, Peter M. Edwards<sup>4</sup>, Jessica B. Gilman<sup>2</sup>, Brian M. Lerner<sup>1,2</sup>, William P. Dubé<sup>1,2</sup>, Michael Trainer<sup>2</sup>, Daniel E. Wolfe<sup>1,5</sup>, Wayne M. Angevine<sup>1,2</sup>, Joost deGouw<sup>2,3</sup>, Eric J. Williams<sup>2</sup>, Alex G. Tevlin<sup>6</sup>, Jennifer G. Murphy<sup>6</sup>, Emily V. Fischer<sup>7</sup>, Stuart McKeen<sup>1,2</sup>, Thomas B. Ryerson<sup>2</sup>, Jeff Peischl<sup>1,2</sup>, John S. Holloway<sup>1,2</sup>, Kenneth Aikin<sup>1,2</sup>, Andrew O. Langford<sup>2</sup>, Christoph J. Senff<sup>1,2</sup>, Raul J. Alvarez II<sup>2</sup>, Samuel R. Hall<sup>8</sup>, Kirk Ullmann<sup>8</sup>, Kathy O. Lantz<sup>1,9</sup>, and Steven S. Brown<sup>2,3</sup>

<sup>1</sup>Cooperative Institute for Research in Environmental Sciences, University of Colorado Boulder, Boulder, Colorado, USA, <sup>2</sup>Chemical Sciences Division, Earth System Research Laboratory, NOAA, Boulder, Colorado, USA, <sup>3</sup>Department of Chemistry, University of Colorado Boulder, Boulder, Colorado, USA, <sup>4</sup>Department of Chemistry, University of York, York, UK, <sup>5</sup>Physical Sciences Division, Earth System Research Laboratory, NOAA, Boulder, Colorado, USA, <sup>6</sup>Department of Chemistry, University of Toronto, Toronto, Ontario, Canada, <sup>7</sup>Department of Atmospheric Science, Colorado State University, Fort Collins, Colorado, USA, <sup>8</sup>Atmospheric Chemistry Observations and Modeling Laboratory, NCAR, Boulder, Colorado, USA, <sup>9</sup>Global Monitoring Division, Earth System Research Laboratory, NOAA, Boulder, Colorado, USA

**Abstract** Tropospheric O<sub>3</sub> has been decreasing across much of the eastern U.S. but has remained steady or even increased in some western regions. Recent increases in VOC and NO<sub>x</sub> emissions associated with the production of oil and natural gas (O&NG) may contribute to this trend in some areas. The Northern Front Range of Colorado has regularly exceeded O<sub>3</sub> air quality standards during summertime in recent years. This region has VOC emissions from a rapidly developing O&NG basin and low concentrations of biogenic VOC in close proximity to urban-Denver NO<sub>x</sub> emissions. Here VOC OH reactivity (OHR), O<sub>3</sub> production efficiency (OPE), and an observationally constrained box model are used to quantify the influence of O&NG emissions on regional summertime O<sub>3</sub> production. Analyses are based on measurements acquired over two summers at a central location within the Northern Front Range that lies between major regional O&NG and urban emission sectors. Observational analyses suggest that mixing obscures any OPE differences in air primarily influenced by O&NG or urban emission sector. The box model confirms relatively modest OPE differences that are within the uncertainties of the field observations. Box model results also indicate that maximum O<sub>3</sub> at the measurement location is sensitive to changes in NO<sub>x</sub> mixing ratio but also responsive to O&NG VOC reductions. Combined, these analyses show that O&NG alkanes contribute over 80% to the observed carbon mixing ratio, roughly 50% to the regional VOC OHR, and approximately 20% to regional photochemical O<sub>3</sub> production.

### 1. Introduction

Tropospheric ozone (O<sub>3</sub>) is a secondary pollutant that contributes to the degradation of regional air quality. The only known sources of tropospheric O<sub>3</sub> are through the intrusion of O<sub>3</sub>-rich stratospheric air [Roelofs and Lelieveld, 1995] and the oxidation of volatile organic compounds (VOCs) in the presence of nitrogen oxides (NO<sub>x</sub> = NO + NO<sub>2</sub>) [Chameides, 1978; Crutzen, 1970]. In the past two decades, summertime maximum O<sub>3</sub> at rural (receptor) sites across much of the U.S. has exhibited a strongly decreasing trend [Cooper et al., 2012], likely in response to concurrent, declining NO<sub>x</sub> emissions [e.g., Butler et al., 2011; Cooper et al., 2012; Environmental Protection Agency, 2016]. Decreasing O<sub>3</sub> trends have been most pronounced in the eastern U.S., but generally more moderate, or even increasing, at high-elevation western sites [Cooper et al., 2012]. Proposed explanations for upward trends include increases in summer temperatures, contributions from stratospheric intrusions, long-range transport of emissions from Asia, western wildfire activity, and/or regional oil and natural gas (O&NG) emissions [Cooper et al., 2012, 2015]. Here we focus on summertime O<sub>3</sub> production impacted by O&NG activity in the Colorado Northern Front Range (NFR) (Figure 1), a region out of compliance with National Ambient Air Quality Standards (NAAQS) of 75 ppbv for O<sub>3</sub> since 2007 and expected to remain so under recently revised 2015 standards of 70 ppbv [Colorado Department of Public Health and Environment (CDPHE), 2016].

The NFR (Figure 1) has urban O<sub>3</sub> precursor emissions in close proximity to those from other sectors, principally agriculture (e.g., animal feedlots) and O&NG production. The NFR's Wattenberg Gas Field of the greater Denver-Julesburg Basin has seen significant recent increases in O&NG production, with the number of active

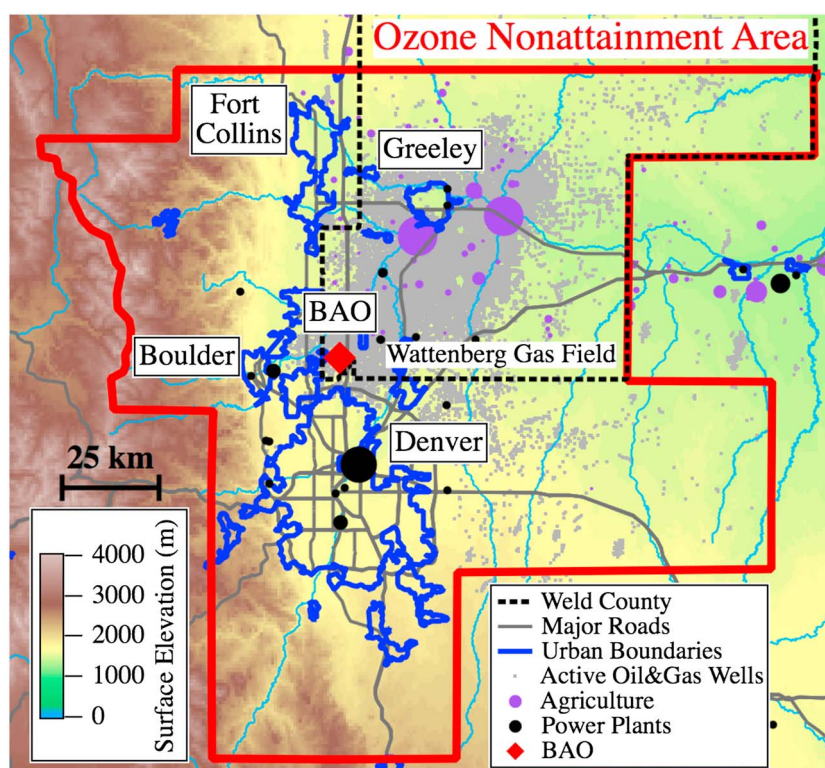


**Figure 1.** Elevation map of the Northern Front Range (NFR) region of Colorado showing the O<sub>3</sub> nonattainment area, Weld County (dashed lines), major roads, rivers, urban regions, power plants (scaled by relative NO<sub>x</sub> emissions), large agricultural facilities (feedlots sized by animal capacity), and active O&NG wells [Colorado Oil and Gas Conservation Commission (COGCC), 1/2016]. The red diamond indicates the location of the BAO measurement site.

wells nearly doubling in Weld County between January 2008 and July 2015 to over 27,000 [Colorado Oil and Gas Conservation Commission (COGCC), 2/2016]. Though O&NG production has increased in multiple U.S. basins, a relatively small number of these basins lie in close proximity to large urban areas, as is the case with the Denver-Julesburg. Biogenic VOC mixing ratios (e.g., isoprene) are relatively low in the NFR compared to other U.S. O&NG producing regions, such as Texas and Pennsylvania [Rutter *et al.*, 2015; Swarthout *et al.*, 2015]. Lower biogenic mixing ratios may magnify the influence of O&NG emissions on regional O<sub>3</sub> production. Multiple studies have extensively characterized NFR VOC emissions, including those from O&NG activity [e.g., Brantley *et al.*, 2015; Gilman *et al.*, 2013; Pétron *et al.*, 2012, 2014; Swarthout *et al.*, 2013], but remain limited in terms of characterizing their influence on summertime O<sub>3</sub> production.

To date, relatively few studies have specifically assessed the influence of emissions associated with O&NG activity on regional summertime O<sub>3</sub> production. Several recent papers have focused on wintertime O<sub>3</sub> in O&NG producing regions in both the Upper Green River Basin of Wyoming [Field *et al.*, 2015; Oltmans *et al.*, 2014; Rappenglück *et al.*, 2014; Schnell *et al.*, 2009] and the Uintah Basin in Utah [Ahmadov *et al.*, 2015; Carter and Seinfeld, 2012; Edwards *et al.*, 2014, 2013; Helmig *et al.*, 2014; Oltmans *et al.*, 2014]. Winter O<sub>3</sub>, however, is distinct from summertime urban-influenced O<sub>3</sub> and has so far only occurred in remote areas with low population densities and urban emissions. Winter O<sub>3</sub> is also specific to highly stable inversion conditions that cause an accumulation of VOC emissions from O&NG activity. The influence of O&NG emissions on summer O<sub>3</sub> near urban areas is not well characterized and is a potentially complex issue arising from the interaction of a variety of emissions.

Previous summertime O<sub>3</sub> analyses include two initial studies that used regional models to determine that O<sub>3</sub> production was positively influenced by emissions associated with O&NG activity in the Haynesville region in Texas [Kemball-Cook *et al.*, 2010] and across multiple western U.S. locations [Rodriguez *et al.*, 2009]. More recent work has suggested that O&NG-associated NO<sub>x</sub> emissions, relative to those of VOCs, contribute disproportionately to summertime O<sub>3</sub> production. For example, O&NG-associated VOC emissions only contribute 8%

to O<sub>3</sub> precursors in California's San Joaquin Valley [Gentner *et al.*, 2014] and less than 20% and 7%, respectively, to the O<sub>3</sub> forming potential in the Barnett Basin near Fort Worth, Texas [Rutter *et al.*, 2015] and Pennsylvania's Marcellus Basin [Swarthout *et al.*, 2015]. Similarly, regional modeling of the Eagle Ford Basin in Texas showed that changes in regional summertime O<sub>3</sub> concentrations were not driven by O&NG-associated VOCs but rather by emissions of NO<sub>x</sub> [Pacsi *et al.*, 2015]. As observed from space, NO<sub>x</sub> levels associated with O&NG activity (e.g., flaring and combustion from O&NG extraction machinery and transport vehicles) have recently increased over three O&NG producing regions in the central U.S. [Duncan *et al.*, 2016]. In other states such as Pennsylvania, the influence of O&NG activity on O<sub>3</sub> may be underestimated or obscured due to (1) NO<sub>x</sub> trends masked by surrounding urban emission reductions [Duncan *et al.*, 2016] and/or (2) gaps in the monitoring network for Environmental Protection Agency (EPA) criteria pollutants, such as NO<sub>2</sub> [Carlton *et al.*, 2014].

Here we apply three methods to characterize the influence of VOC and/or NO<sub>x</sub> emissions on O<sub>3</sub> production in the NFR. These include VOC OH reactivity (OHR), O<sub>3</sub> production efficiency (OPE), and photochemical box modeling. The VOC OH reactivity (OHR) [e.g., Gilman *et al.*, 2013] is a measure of the kinetic oxidation of VOCs by the OH radical and is often the rate limiting step in photochemical O<sub>3</sub> production. A number of O&NG-focused studies have used this metric to highlight the potential contribution of O&NG VOCs to O<sub>3</sub> production in both summer and winter months [Field *et al.*, 2015; Gilman *et al.*, 2013; Rutter *et al.*, 2015; Swarthout *et al.*, 2013, 2015]. Although VOC OHR provides a simple assessment of the relative contribution of different VOCs to potential O<sub>3</sub> production, it does not incorporate information about radical propagation or its NO<sub>x</sub> dependence, both of which are important for predicting the efficiency of O<sub>3</sub> production. Ozone production efficiency (OPE) [e.g., Trainer *et al.*, 1993] is a measure of the number of O<sub>3</sub> molecules produced, or number of NO<sub>x</sub> interconversion cycles completed, before NO<sub>x</sub> is lost through termination reactions (e.g., nitric acid (HNO<sub>3</sub>) or organic nitrate production). The OPE is defined as the slope of odd oxygen (O<sub>x</sub> = NO<sub>2</sub> + O<sub>3</sub>) plotted against NO<sub>z</sub> (NO<sub>z</sub> = NO<sub>y</sub> - NO<sub>x</sub>, where NO<sub>y</sub> is total oxidized reactive nitrogen). OPE analyses have been used to characterize urban and rural regions across the U.S. as documented in Table 1 of Griffin *et al.* [2004], but to our knowledge, have not been applied specifically to O<sub>3</sub> production in an O&NG basin. The principle advantage to OPE is that it is an observable quantity that should differentiate between air parcels of different VOC composition and NO<sub>x</sub> mixing ratios, for example, those influenced by O&NG versus urban emissions. However, OPE derived from field observations is an upper limit as it suffers from artifacts such as depositional NO<sub>y</sub> loss.

Box model analyses are a common tool used to assess the sensitivity of O<sub>3</sub> production to NO<sub>x</sub> and VOC emissions within air parcels of known composition. They have been used recently to model O<sub>3</sub> production in western U.S. O&NG basins during winter months [Carter and Seinfeld, 2012; Edwards *et al.*, 2013, 2014]. To our knowledge, a box model analysis has not been previously reported for summertime O<sub>3</sub> production in an O&NG basin. Box models have the advantage of a fully explicit chemical mechanism, but they parameterize transport as a highly simplified, single dilution term. They therefore do not represent heterogeneity in the spatial distribution of emissions. They also do not rely on emission inventories, which can be an important source of uncertainty in three-dimensional chemical transport models [e.g., Ahmadov *et al.*, 2015], but parameterize emissions so as to match observations or constrain primary species to observed values. Box model analyses are useful in assessing the NO<sub>x</sub> and VOC sensitivities of O<sub>3</sub> and other secondary products (e.g., acetone, MEK, and RONO<sub>2</sub>) for averaged data, in which chemical and meteorological variabilities average to typical values [Edwards *et al.*, 2013], or in simulations of air parcel evolution along a known trajectory [Washenfelder *et al.*, 2011b]. In these cases, box models provide a simple alternative to 3-D chemical transport models.

We present a combination of VOC OHR and OPE analyses along with an observationally constrained box model to (1) quantify the impacts of O&NG emissions on summertime maximum O<sub>3</sub> and its production efficiency at a specific location within the NFR and (2) evaluate the O<sub>3</sub> sensitivity to NO<sub>x</sub> and VOC emissions. This analysis indicates that the influence of O&NG VOCs on regionally produced O<sub>3</sub> is small relative to their contribution to total VOC mass and OHR, but not negligible on the scale relevant to attainment of regional air quality standards.

## 2. Experimental and Analysis Methods

### 2.1. Measurement Site

The Boulder Atmospheric Observatory (BAO; 40.05°N, 105.01°W, 1584 m above sea level) [Kaimal and Gaynor, 1983] lies roughly 35 km north of Denver and 25 km east of Boulder in the southwest corner of the

Wattenberg Gas Field (Figure 1). The site has a tall (300 m) tower with south facing stationary platforms (booms) at 10, 100, and 300 m for meteorological measurements of temperature, relative humidity, wind speed, and direction. An external carriage mounted on the southwest side of the tower provides a platform for vertically resolved chemical measurements as described further in section S1 in the supporting information.

## 2.2. Field Campaigns

Measurements at BAO were made in July–August 2012 and July–August 2014, months when the NFR experiences  $O_3$  levels in exceedance of the EPA 8 h  $O_3$  standard [Colorado Department of Public Health and Environment (CDPHE), 2015]. During these two summers, the NFR was studied by three major field campaigns that contributed data to this analysis. Campaign and measurement descriptions can be found below and as a complete list in Table S1 in the supporting information.

### 2.2.1. SONNE: 2012

The Summer Ozone Near Natural gas Emissions (SONNE) field campaign was conducted at BAO between 27 July and 12 August 2012. Chemical measurements were acquired via inlets mounted 8 m above ground level (agl) on a walkup tower ~10 m south of the main tower. Continuous in situ measurements of a full suite of  $C_2$ – $C_{10}$  hydrocarbons,  $C_2$ – $C_4$  oxygenated VOCs, aromatics,  $C_2$ – $C_3$  alkyl nitrates, and dimethyl sulfide were collected via a custom-built, two-channel gas chromatograph-mass spectrometer (GC-MS) [Gilman *et al.*, 2010]. Samples were acquired (5 min) and analyzed (25 min) on a repeating cycle every 30 min. The accuracy and detection limits are compound-dependent but less than 25% and 10 parts per trillion by volume (pptv), respectively [Gilman *et al.*, 2010].  $NO_x$  and  $NO_2$  were measured with a custom-built, multichannel cavity ring-down (CRD) instrument.  $NO_2$  was measured by direct absorption at 405 nm, while  $NO_x$  was simultaneously measured in a second channel after conversion of ambient NO to  $NO_2$  via an addition of excess  $O_3$  [Fuchs *et al.*, 2009]. The accuracy and limit of detection for both species were <5% and <30 pptv, respectively.  $O_3$  was measured via UV absorbance by a commercial instrument (Thermo Environmental Instruments, Inc., Model 49c). Methane ( $CH_4$ ) was measured via CRD spectroscopy using a wavelength-scanned CRD instrument (Picarro, model 1301 m) [Peischl *et al.*, 2012]. Carbon monoxide (CO) was measured by a vacuum ultraviolet fluorescence instrument [Gerbig *et al.*, 1999]. All chemical measurements were collected at a 1 Hz time resolution and averaged to the GC-MS acquisition period of 5 min every half hour.

### 2.2.2. FRAPPÉ/DISCOVER-AQ: 2014

In July–August 2014 the NSF Front Range Air Pollution and Photochemistry Experiment (FRAPPÉ) and the NASA Deriving Information on Surface Conditions from Column and Vertically Resolved Observations Relevant to Air Quality (DISCOVER-AQ) field campaigns conducted aircraft, mobile, and ground-based measurements at over 15 locations across the Front Range. Measurements at BAO took place between 16 July and 15 August 2014 and included surface and vertically resolved observations.  $CH_4$  and CO were measured from the instrument carriage with a commercial CRD instrument (Picarro, model 2401) [Chen *et al.*, 2010, 2013; Crosson, 2008]. Gas-phase ammonia ( $NH_3$ ) was measured from the carriage via infrared absorption with a quantum-cascade laser instrument (QC-TILDAS) [McManus *et al.*, 2008].  $NO_x$  and  $NO_2$  were measured with the same CRD instrument described in section 2.2.1, which also measured  $O_3$  and  $NO_y$ .  $O_3$  was measured by conversion to  $NO_2$  in excess NO and subsequent subtraction of ambient  $NO_2$  from the resulting total  $O_x$  [Washenfelder *et al.*, 2011a].  $NO_y$  was thermally converted to NO or  $NO_2$  with a quartz heater (650°C) and quantitatively converted to  $NO_2$  via an addition of  $O_3$  [Wild *et al.*, 2014]. The accuracy and detection limit of  $NO_x$ ,  $NO_2$ , and  $O_3$  in 2014 were <5% and <50 pptv, respectively. The  $NO_y$  channel had a limit of detection of <200 pptv and an accuracy of 12% based on recent field comparisons to other  $NO_y$  instruments [Wild *et al.*, 2014]. Conversion of  $NO_y$  in a 650°C quartz oven may have also suffered interference from the unintended conversion of a small fraction (~6%) of  $NH_3$  in the presence of  $O_3$ . Uncertainty associated with this artifact is estimated for the  $NO_y$  data based on co-located  $NH_3$  and  $O_3$  measurements, but data are not corrected for this potential interference.

In addition to carriage instruments,  $O_3$  lidar (NOAA TOPAZ) [Alvarez *et al.*, 2011; Langford *et al.*, 2015] measurements were made at a ground site ~0.5 km south of the main tower and  $j(NO_2)$  photolysis frequencies (National Center for Atmospheric Research (NCAR) filter radiometer [Shetter *et al.*, 2003]) were measured from a trailer parked at the tower base. Lastly, spectral surface albedo measurements derived from a visible (415–1625 nm) Multi-Filter Rotating Shadowband Radiometer [Harrison *et al.*, 1994; Michalsky and Hodges,

2013] were made from a NOAA Surface and Radiation Budget Monitoring mobile laboratory [Augustine et al., 2000] parked at BAO for the duration of the campaign.

### 2.3. Ozone Production Efficiency

Ozone production efficiencies were only derived from 2014 data due to the lack of  $\text{NO}_y$  measurements in 2012. Chemical observations were averaged to a 1 min time resolution and filtered to include data after noon (12–6 P.M. mountain daylight time (MDT)) during peak  $\text{O}_3$  production and sampling altitudes  $>25$  m agl to reduce the influence of deposition to the surface. The slope of the  $\text{O}_x$  to  $\text{NO}_z$  correlation at individual, 15 min intervals was used to isolate and derive the OPE of individual air parcels. In contrast to the  $\text{O}_3/\text{NO}_z$  slope defined in previous studies [e.g., Hirsch et al., 1996; Olszyna et al., 1994; Trainer et al., 1993, 1995], the use of  $\text{O}_x$  accounts for local  $\text{O}_3$  titration through reaction of  $\text{NO}$  with  $\text{O}_3$  near  $\text{NO}_x$  emission sources. Additionally,  $\text{NO}_z$ , instead of  $\text{NO}_y$ , normalizes age across different air parcels [Trainer et al., 1993]. However, by not additionally accounting for  $\text{NO}_y$  removal processes, such as surface deposition of individual  $\text{NO}_y$  species (e.g.,  $\text{HNO}_3$ ), the OPEs derived here are upper limits. Further OPE details are discussed in sections 3.3 and S2.

### 2.4. Box Model

#### 2.4.1. Model Description and Constraints

Model simulations were performed with the Dynamically Simple Model of Atmospheric Chemical Complexity (DSMACC) [Emmerson and Evans, 2009]. DSMACC is a zero dimension box model that uses the Master Chemical Mechanism (MCM v3.3.1) for its chemistry scheme and the NCAR Tropospheric Ultraviolet and Visible Radiation Model (TUV v5.2) [Madronich et al., 1998] for photolysis rates. The MCM is a near-explicit chemical mechanism representing the gas-phase tropospheric degradation of VOCs [Jenkin et al., 2015]. The subset of chemistry used here includes a complete inorganic mechanism and degradation scheme for 50 primary VOCs, with a total of 4002 species and 15,555 reactions.

All DSMACC simulations are initialized at 8 A.M. MDT and integrated forward for 24 h with a 10 min time step. To represent the NFR as a photochemical box, simulations are initialized with and constrained every 30 min to SONNE diel average observations of temperature and mixing ratios of  $\text{CO}$ ,  $\text{CH}_4$ , 42 non-methane VOCs, and water vapor (derived from 10 m relative humidity measurements). Simulations are constrained to 2012 data only due to lack of speciated VOC measurements in 2014. For comparison, both temperature and observed  $\text{O}_3$  mixing ratios were higher in 2012 than 2014 with differences in maximum diel averages (27 July to 12 August 2012 and 2014) of  $1^\circ\text{C}$  and 1.8 ppbv, respectively. DSMACC simulations were additionally constrained to SONNE diel average observations of total  $\text{NO}_x$ , which was partitioned by the model into its components ( $\text{NO}$  and  $\text{NO}_2$ ) every 10 min assuming photo-stationary state, using  $j(\text{NO}_2)$ , temperature, and  $\text{O}_3$ . Section S3 provides further information on DSMACC constraints, which force the model to accurately represent primary species whose average concentrations are governed by processes not represented in the box model, such as emissions and horizontal transport.

An additional dilution rate constant was applied to all 4002 model compounds to simulate average vertical transport and loss from the box (as described in section S3.3). A dilution rate constant of  $1.05 \times 10^{-4} \text{ s}^{-1}$  was derived from a fit of the model output to the diel average observations of 10 secondary products. These 10 secondary species consist of  $\text{O}_3$ , six oxygenated VOCs, and three alkyl nitrates, which were initialized to their average observed values (8 A.M. MDT) but not otherwise constrained (see Figure S6). Background mixing ratios of these 10 compounds (Table S3) were also added to the model at the same rate of dilution to account for entrainment and mixing with the residual layer during boundary layer growth. At the fit dilution rate, the average model-to-observation difference for all 10 compounds was  $-13.7\%$  (for individual compounds, see Table S3). Table S2 summarizes the model treatment of all chemical observations, and Figure 2 illustrates the observed non-methane VOCs in terms of their diel average OHR.

#### 2.4.2. Model Scenarios

Base (Case 1) simulations represent the average chemical composition at BAO and were constrained to diel average chemical and physical observations as described above. In comparison with Case 1 simulations, Cases 2 and 3 (described below) are used to quantify the impact of primary O&NG VOCs on maximum photochemical  $\text{O}_3$  production.

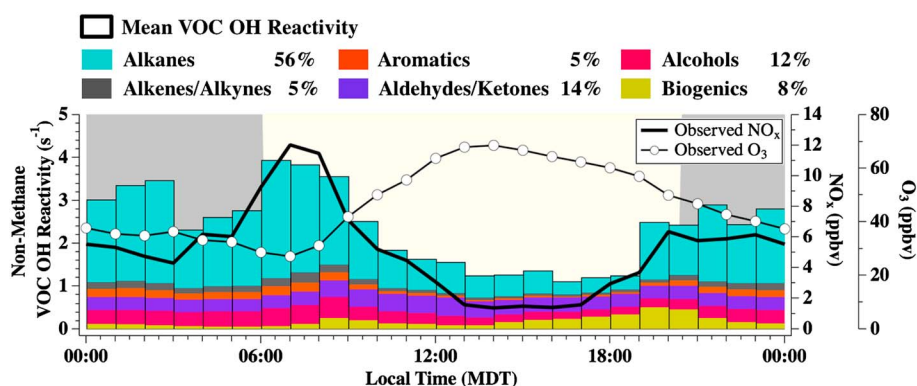


**Figure 2.** Diel average of non-methane VOC and  $\text{NO}_x$  model constraints. VOCs (left axis) are given in VOC OH reactivity;  $\text{NO}_x$  and  $\text{O}_3$  (right axes) are given in mixing ratio. The bar height is the average VOC OHR colored by the fractional VOC class contribution every 60 min. Average VOC class contributions are calculated from the sum of averaged (24 h) individual VOCs. VOC OHR does not include contributions from HCHO, CO, or  $\text{CH}_4$ . Aldehydes and ketones shown here were not used as model constraints but instead used to derive the dilution rate constant.

Case 2 simulations represent the average chemical composition at BAO without primary O&NG VOCs. To derive this VOC scenario, speciated fractions of primary VOCs emitted from O&NG activity were subtracted from Case 1 diel average observations. For example, propane was reduced by 90% between Cases 1 and 2, as 90% of observed propane at BAO was attributed to O&NG emissions [Gilman *et al.*, 2013]. Table S2 provides a full list of speciated O&NG contribution factors. For all non-methane VOCs, Gilman *et al.* [2013] used a multivariate regression with O&NG (propane) and urban (acetylene) tracers to derive O&NG factors. Oxygenated VOCs were not tightly correlated with either tracer and were not assigned an O&NG factor by Gilman *et al.* [2013]. Here the O&NG factors for these compounds have been set to 0%, resulting in a conservative (lower limit) estimate for the attributed O&NG fraction of observed VOCs. In addition, three cycloalkanes, two alkenes, one aldehyde, three biogenic VOCs, and three alkyl nitrates measured during SONNE were not reported by Gilman *et al.* [2013] and are also assigned an O&NG contribution of 0%. The cycloalkanes likely have an O&NG source but minimally impact simulated  $\text{O}_3$  due to their small mixing ratios ( $<0.03$  ppbv) and nonexplicit representation in the MCM (section S3.1). For all additional species measured but not explicitly represented in the MCM (see section S3.1), factors were applied to each individual compound prior to lumping. As illustrated in Figure 3, primary O&NG emissions contributed to the majority of alkane OHR (87%) and carbon mixing ratio (86%), but  $<25\%$  to all other VOC classes. For  $\text{CH}_4$ , Pétron *et al.* [2014] quantified the O&NG contribution in the Wattenberg Gas Field as 75% using a combination of aircraft  $\text{CH}_4$  observations and a regional bottom-up emission inventory (derived from literature emission factors, Colorado State inventory data, and EPA reported facility-level emission estimates). Here 75% is applied to the observed average diel profile of enhanced  $\text{CH}_4$  (minus campaign background of 1814 ppbv). For  $\text{NO}_x$ , no contribution from O&NG activity was assumed. County level  $\text{NO}_x$  emissions based on the 2011 (v1) U.S. National Emissions Inventory (further details in section S4) suggest an O&NG contribution of 5.5% to  $\text{NO}_x$  emissions in the NFR nonattainment area (Figure 1). Past work in a Utah O&NG basin has shown that  $\text{NO}_x$  emissions from O&NG production can be overestimated by a factor of 4 [Ahmadov *et al.*, 2015], indicating that the 5.5% contribution of O&NG activity to NFR  $\text{NO}_x$  emissions may be an upper limit.

Case 3 simulations represent the average BAO chemical composition with a doubled contribution from primary O&NG VOCs. For Case 3, speciated factors for primary O&NG VOCs (as described above) were added to Case 1 diel observations. Table S4 provides a numeric comparison of all three VOC scenarios in terms of their non-methane VOC OHR and carbon mixing ratio (ppbC).

### 3. Results and Discussion

#### 3.1. Observed Chemical Composition and Wind Patterns

Air composition at BAO contains chemical tracers from all regional emission sectors (e.g., O&NG, urban, and agriculture), irrespective of wind direction. The histogram in Figure 4b plots simple chemical tracers for all

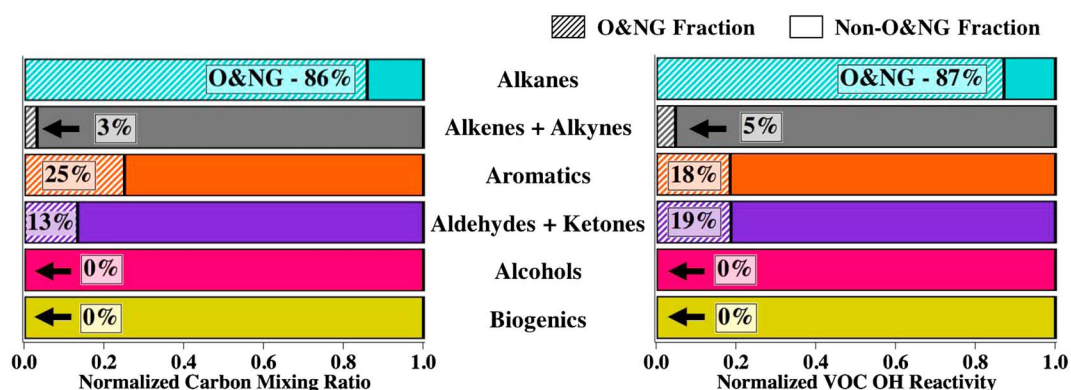


**Figure 3.** O&NG fraction of observed non-methane VOCs as a function of normalized carbon mixing ratio and VOC OH reactivity. Note that aldehydes and ketones were initialized with Case 1 mixing ratios (assuming O&NG VOC fraction = 0) and calculated by DSMACC in all simulations. The aldehyde and ketone O&NG fractions (OHR: 19% and ppbC: 13%) were derived from a comparison of the Case 1 VOC scenario with the removed O&NG scenario (Case 2) at 2012 observed NO<sub>x</sub> mixing ratios.

major emission sectors (O&NG, CH<sub>4</sub>; agriculture, NH<sub>3</sub>; and urban, CO and NO<sub>x</sub>), averaged between 2012 and 2014 observation years, binned by wind direction, and normalized to westerly mixing ratios. Data have been binned by four wind directions and filtered to include wind speeds >2.5 m/s to minimize the influence of nearby emission sources and to be consistent with the threshold used by Pétron *et al.* [2012]. Figure 4b shows that air at the site has a substantial contribution from all regional emission sources irrespective of local north, east, or southerly wind directions. In addition, enhancements of tracers in the direction of each major emission source (e.g., NO<sub>x</sub> is slightly enhanced in southerly winds) are smaller than those observed in wintertime [Brown *et al.*, 2013, Figure 7]. These observations suggest significant mixing and recirculation that causes regional air to have characteristics of all surrounding emission sectors.

Several mechanisms serve to mix emissions from different sources within the NFR. During summer, winds follow a typical mountain-valley diel pattern. During the day, thermally driven upslope winds predominately flow from the east, with a slight southerly component [Toth and Johnson, 1985]. Beginning in late afternoon, flow patterns turn around and a westerly downslope occurs along the South Platte River Basin, often accompanied by afternoon regional thunderstorm activity [Toth and Johnson, 1985]. Figure 4a provides a histogram of 30 min averaged winds measured at BAO during July and August 2012 and 2014 (100 m winds, speed >2.5 m/s, 11 A.M. to 3 P.M. MDT), which illustrate this dominant afternoon easterly flow prior to the downslope switch. A terrain-forced mesoscale vortex circulation pattern, termed the Denver Cyclone, is also a common occurrence during summer months [Crook *et al.*, 1990; Szoke, 1991; Szoke *et al.*, 1984; Wilczak and Glendening, 1988]. These complex circulation patterns combine to mix air parcels, making it difficult to model the daily evolution of emissions from spatially distinct regional emission source sectors.

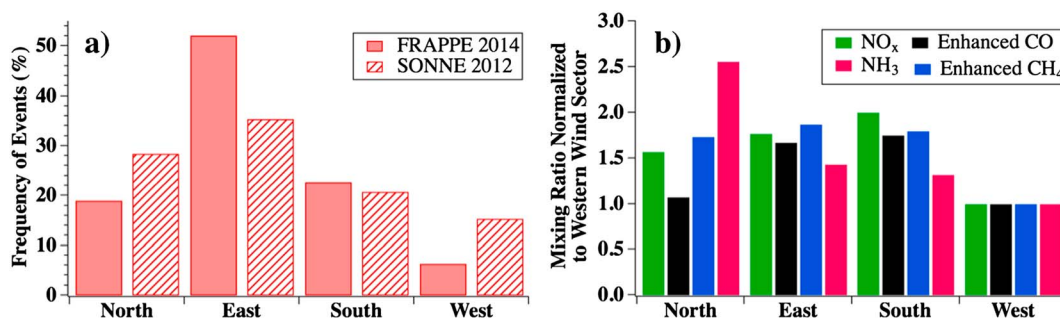


**Figure 4.** (a) Histogram of July–August 2012 and 2014 wind direction measured at BAO (100 m). (b) Median mixing ratios of chemical tracers averaged between 2012 and 2014 campaign years, normalized to mixing ratios in the western wind sector to illustrate relative sector-to-sector differences on the same scale for all species. CO and CH<sub>4</sub> plotted as normalized enhancements above observed 2012 and 2014 backgrounds. All data filtered for wind speeds of >2.5 m/s. Binned wind directions correspond to north: 315°–45°, east: 45°–135°, south: 135°–225°, and west: 225°–315°.

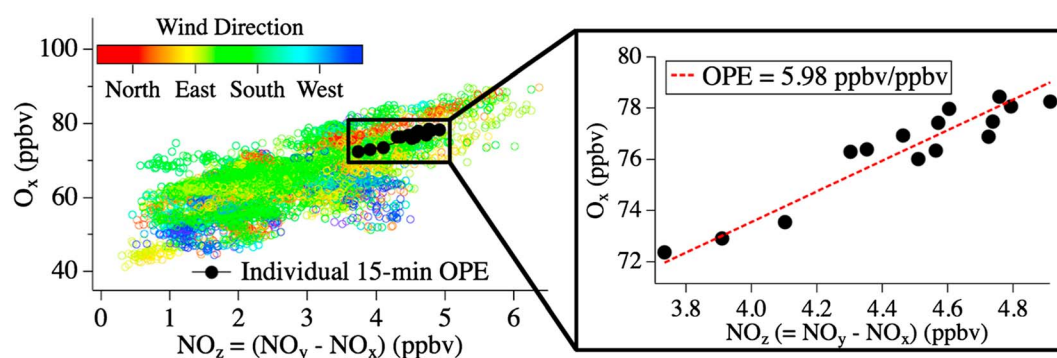


**Figure 5.** (left) Observed  $O_x/NO_z$  correlation for 16 July to 15 August 2014 (12 P.M. to 6 P.M. MDT,  $N = 8268$ ), colored by observed wind direction. (right) Example  $O_x/NO_z$  correlation during one, 15 min time interval. This OPE meets the point number ( $>11$ ), intercept ( $56.7 \pm 9.3$  ppbv), and  $r^2$  ( $>0.5$ ) filter requirements discussed in text.

### 3.2. VOC OH Reactivity: 2012

The campaign average ( $\pm 1\sigma$  standard deviation) OHR for non-methane VOCs (excluding HCHO) observed during SONNE was  $2.4 \pm 0.9 \text{ s}^{-1}$ . This compares to a previous determination at BAO of  $3 \pm 3 \text{ s}^{-1}$  based on an analysis of data from same instrument in winter 2011 [Gilman *et al.*, 2013] and summertime measurements near O&NG operations in Pennsylvania of  $2.4 \pm 1.4 \text{ s}^{-1}$  (includes  $CH_4$ , excludes HCHO) [Swarthout *et al.*, 2015]. On average, alkanes were the dominant contributing class to VOC OHR (56%; Figure 2), of which the majority can be attributed to primary O&NG emissions (87%; VOC OHR, 86%; ppbC; Figure 3). Biogenic VOCs have been shown to dominate VOC OHR in O&NG regions in Pennsylvania ( $47 \pm 22\%$  [Swarthout *et al.*, 2015]) and Texas (70% [Rutter *et al.*, 2015]), but only contribute on average, 8% to VOC OHR at BAO. This result highlights the importance of O&NG emissions relative to biogenic emissions on  $O_3$  production in the NFR, making this location unique compared to two east/southeastern U.S. O&NG basins.

### 3.3. Ozone Production Efficiency: 2014

During the 2014 campaign, afternoon  $O_x$  was correlated with  $NO_z$  (Figure 5), typical of summertime relationships between  $O_3$  and oxidized reactive nitrogen observed in other U.S. regions [e.g., Trainer *et al.*, 1993]. Individual OPEs were derived from a two-sided regression fit of  $O_x$  to  $NO_z$  every 15 min between 12 and 6 P.M. MDT after removing time intervals with fewer than 11, 1 min data points. This time period was chosen to minimize the effects of nonphotochemical factors such as morning  $O_3$  entrainment (see section S2.3.2) and to compare the products of photochemistry (i.e.,  $NO_z$  and  $O_3$ ) in distinct air parcels. Increasing the time period to 9 A.M. to 6 P.M. MDT introduces additional scatter in the data from the OPE analyses but does not change the main conclusions presented below. Further, fits with intercepts more than  $\pm 2\sigma$  from the mean intercept were also removed, as described further below and in section S2.2. There were 305 OPE fits that met these criteria, which represent at least 15 min of 27 (87%) afternoons in 2014 (see Figure S1). The average ( $\pm 1\sigma$ ) of these 305 OPEs was  $2.9 \pm 4.4$  ppbv/ppbv.

To ensure at least a 98.4% (i.e., significant) probability of correlation, a subset of these OPEs with correlation coefficients ( $r^2$ )  $> 0.5$  was also selected. There were 80 OPEs that met the  $r^2$  threshold, which represent at least 15 min of 22 (71%) afternoons in 2014 (see Figure S1). The average ( $\pm 1\sigma$ ) of this 80 OPE subset was  $5.3 \pm 3.6$  ppbv/ppbv. Selection of this subset reduced scatter in the data but also introduced a high bias by eliminating data scattered close to zero (e.g., with small changes in  $O_x$  and/or  $NO_z$ ). We take this smaller 80 OPE subset to represent time periods with the greatest photochemical  $O_3$  production but compare both 305 and 80 OPE populations below. Both populations are representative of the majority of high ( $>70$  ppbv)  $O_3$  days observed at BAO in 2014.

Average OPEs ( $\pm 1\sigma$ ) derived here are similar to those from analyses in other regions of the U.S. However, many previous studies have defined OPE as the slope of  $O_3/NO_z$  or  $O_3/NO_y$ , making it difficult to directly compare values here to much of the past  $\sim 20$  years of OPE literature. Nevertheless, the averages of 2.9 ppbv/ppbv (305 OPEs) and 5.3 ppbv/ppbv (80 OPEs) fall within the range of 2–8 ppbv/ppbv for  $O_x/NO_z$  previously reported for urban regions across the U.S. [Kleinman *et al.*, 2002; Nunnermacker *et al.*, 1998; St. John *et al.*, 1998; Zaveri *et al.*, 2003].

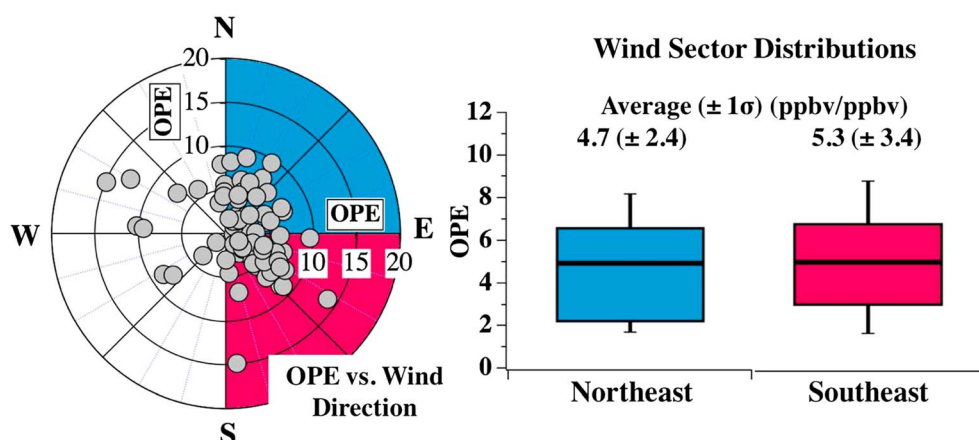


**Figure 6.** 80 individual OPEs with high ( $r^2 > 0.5$ )  $O_x/NO_x$  correlation plotted radially as a function of wind direction, colored by NE (0–90°, blue) and SE (90–180°, red) wind sectors. The box and whisker plots show the median OPE for each wind sector (SE: 5.1 ppbv/ppbv, NE: 4.9 ppbv/ppbv) and range between the 10th and 90th percentiles.

### 3.3.1. NFR Emission Sector OPEs

To distinguish the influence of different emission sectors on OPE, individual OPEs were sorted according to two markers of air transport history: (1) wind direction and (2) simple chemical tracers. Sorting the data according to these markers contrasts the  $O_3$  production associated with the relatively different VOC composition and  $NO_x$  mixing ratios of O&NG and urban emission sectors. As this section describes, however, any dependence of OPE on these parameters is considerably smaller than the variability and/or uncertainty in the observed OPE data.

#### 3.3.1.1. OPE as a Function of Wind Direction

Air arriving at BAO from the northeast is expected to have traveled over regional O&NG operations, while that from the southeast to have been relatively more urban influenced (Figure 1). However, the OPE measured at BAO does not vary strongly with wind direction. The overall  $O_x/NO_x$  correlation in 2014, colored by wind direction (Figure 5, left), does not show a clear difference in air arriving from south or north of the site. Analysis of individual OPEs against wind direction reveals similar results. Figure 6 provides a wind rose of the 80 OPE subset ( $r^2 > 0.5$ ) colored by northeast (NE: 0–90°), southeast (SE: 90–180°), and western (W: 180–360°) wind directions (15 min average). The box and whisker plots for NE and SE wind sectors show no statistically significant (i.e.,  $p > \alpha$ ,  $\alpha = 0.05$ ) difference in their average (difference = 0.6 ppbv/ppbv,  $p = 0.43$ ) or median (difference = 0.1 ppbv/ppbv,  $p = 0.88$ ) values. In addition, there is no significant difference between average NE and SE OPEs (difference = 0.5 ppbv/ppbv,  $p = 0.39$ ) when calculated from the larger population of 305 without the  $r^2$  selection. Due to the large observed variability in OPE, 95% confidence intervals for differences in mean NE and SE OPEs are  $0.6 \pm 1.4$  ppbv/ppbv and  $0.5 \pm 1.1$  ppbv/ppbv for the 80 and 305 OPE populations, respectively. This wind direction analysis suggests a 95% probability that the OPE influence of O&NG emissions is less than 1.8 ppbv/ppbv. During times of high photochemical activity in 2014 (e.g., highest  $NO_x$  mixing ratios; Figure 5), an OPE less than 1.8 ppbv/ppbv suggests that the O&NG sector contributes at most 11 ppbv to total  $O_3$ . The actual O&NG influence determined from the box model analysis is likely considerably smaller (see section 3.4.2).

Due to the complexity of local air trajectories, including diel flow patterns that mix urban and O&NG emissions (section 3.1), it is difficult to accurately determine air transport and mixing histories using observed wind directions alone. A back trajectory model has the potential to track air transport history more accurately than local wind direction. As with observed wind direction, wind sectors for the 80 OPE subset as defined by a back trajectory model (described in section S5) show no statistically significant difference between average OPEs from the NE and SE wind sectors (difference = 0.6 ppbv/ppbv,  $p = 0.55$ ; Figure S9).

The lack of statistically significant difference in observed OPE with observed or modeled wind direction is evidence for mixing between air parcels that obscures quantifiable differences between urban and O&NG sectors and/or an OPE effect from O&NG emissions that has a 95% probability of being less than 1.8 ppbv/ppbv. We interpret these results to mean either (1) observed OPEs are the product of both urban and O&NG emissions that were well-mixed prior to measurement at BAO or (2) an OPE influence of urban and O&NG emissions that are similar enough (i.e.,  $< 1.8$  ppbv/ppbv) to be obscured by mixing when air is transported to BAO.

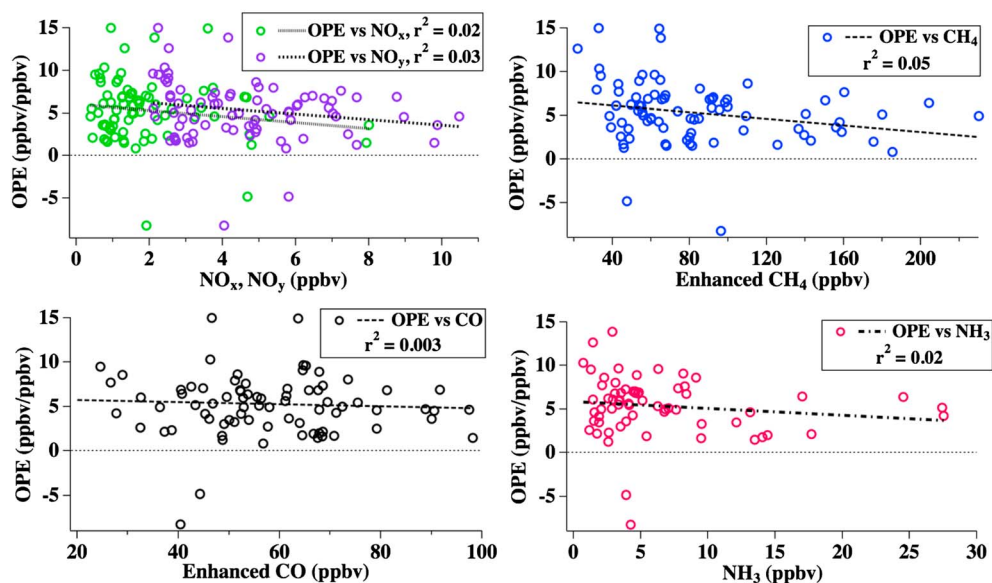


**Figure 7.** 80 individual OPEs with high ( $r^2 > 0.5$ )  $O_x/NO_z$  correlation as a function of simple chemical tracers.  $CH_4$  and CO mixing ratios are the enhancements above background. Correlation coefficients ( $r^2$ ) for all species suggest no statistically significant trend (95% confidence level) in OPE with tracers.

The box modeling results discussed in section 3.4.3 are consistent with the second scenario and suggest an O&NG influence on regional average OPE of 1.3 ppbv/ppbv.

### 3.3.1.2. OPE as a Function of Chemical Tracers

Chemical tracers provide an additional method to determine air transport history. In the NFR,  $CH_4$  is emitted primarily by O&NG (see above section 2.4.2),  $NH_3$  by agriculture, and CO and  $NO_x$  by urban activity. Background mixing ratios (minimum observed campaign values) of CO (76 ppbv) and  $CH_4$  (1916 ppbv) were subtracted prior to analysis. Figure 7 shows correlations of the 80 OPE subset with  $NO_x$ ,  $NO_y$ ,  $NH_3$ ,  $CH_4$ , and CO. Correlations visually indicate a slight decrease in OPE with increasing tracer mixing ratios; however, correlation coefficients indicate no statistically significant trend at the 95% confidence level ( $p > 0.05$ ). Correlations between chemical tracers and the 305 OPE-population are also insignificant ( $p > 0.22$ ). These results indicate relatively well-mixed air, also suggested by the dominant easterly flow and nondirectionally enhanced tracer mixing ratios shown in Figure 4.

A second possibility is that these tracers are not specific enough to their assigned emission sectors. As previously discussed in Pétron *et al.* [2012, 2014], approximately 25% of  $CH_4$  emissions are not associated with O&NG operations, including three landfills located approximately 3 km to the south-southwest of BAO. In addition, NEI-2011 inventories attribute 27% of  $NO_x$  emissions in Weld County (Figure 1) to O&NG operations (section S4). Ideally, this analysis would be conducted with more specific chemical tracers not available in 2014 (e.g., O&NG: propane and urban: acetylene) but suggests that simple tracers used here do not uniquely distinguish the influence of different emission sectors on observed OPE at BAO.

### 3.3.2. Uncertainty in OPE Analysis

Interpretation of the  $O_x/NO_z$  relationship is subject to several limitations [Ryerson *et al.*, 1998; Trainer *et al.*, 1993] that are presented below in terms of their relation to deriving an average OPE under NFR conditions.

First, variability in background  $O_3$  may complicate OPE analysis [e.g., Neuman *et al.*, 2009]. Backgrounds are represented by the intercept of the  $O_x/NO_z$  correlation and will artificially change the OPE if one fit is applied to air parcels with different backgrounds (see example Figure S2). Therefore, OPE was derived from short time intervals (15 min) and filtered for intercepts greater than  $2\sigma$  from the mean  $O_x$  background (further details in section S2.2) in order to isolate air parcels with similar  $O_3$  backgrounds.

Second,  $O_x$  is not always positively correlated with  $NO_z$ . This is likely the result of (1) environmental conditions that do not promote photochemical activity and/or (2) transport processes that mix air parcels with differences in background  $O_3$  mixing ratios similar to their photochemical  $O_3$  enhancements.

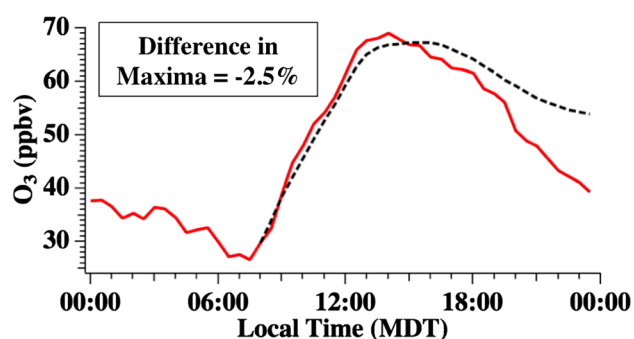


**Figure 8.** Base case (Case 1) simulated  $O_3$ . Observed diel average (red) and Case 1 simulated (black dashed) mixing ratios. Difference between observed and modeled maxima is  $-2.5\%$ .

air parcels remove any observable  $O_x/NO_z$  correlation. The  $r^2$  filter is applied to remove these events but by doing so, biases the 80-OPE average high.

Third, OPE is sensitive to  $HNO_3$  deposition [e.g., Neuman *et al.*, 2009; Sillman *et al.*, 1998; Trainer *et al.*, 1993]. Preferential removal of  $HNO_3$  relative to  $O_3$  will artificially raise the  $O_x/NO_z$  slope since  $HNO_3$  is frequently the largest  $NO_z$  component in summer. A deposition velocity of  $1\text{--}5\text{ cm s}^{-1}$  within a 2 km boundary layer provides an upper limit estimate of 11–52% of  $NO_z$  lost over 6 h of transport (further details, see section S2.3.1). Recalculating individual OPEs with corrected  $NO_z$  produces an average ( $\pm 1\sigma$ ) OPE range of 3.3 ppbv/ppbv ( $\pm 2.2$ ) to 4.7 ppbv/ppbv ( $\pm 3.2$ ) for the highly correlated 80-OPE subset, lower than the original average of 5.3 ppbv/ppbv but within the standard deviation of 3.6 ppbv/ppbv. Additional, unintended conversion of  $NH_3$  may also occur in the presence of ambient  $O_3$  at temperatures of  $650^\circ\text{C}$  in the CRD  $NO_y$  quartz oven. Adjusting  $NO_z$  measurements of the original 80 OPEs with concurrent  $NH_3$  and  $O_3$  measurements (further details in section S2.3.1) increases the average to 5.9 ppbv/ppbv. Combination of  $HNO_3$  and  $NH_3$  artifacts suggests that the average OPE for the highly correlated subset is between 3.3 and 5.9 ppbv/ppbv ( $-2.0/+0.6$ ), a range encompassed by the standard deviation ( $1\sigma = 3.6\text{ ppbv/ppbv}$ ) of the originally derived average.

An analysis of the 2014 data provides an average and expected distribution of observed OPE at BAO but does not distinguish the influence of urban emissions from the O&NG sector. This result does not change with the selection of highly correlated OPEs. These observations lead to three possible conclusions: (1) based on observational and modeled-wind direction analyses, the OPE difference between O&NG and urban emission sectors has a 95% probability of being within 1.8 ppbv/ppbv; (2) OPE differences are obscured by regional air mixing; and/or (3) small OPE differences cannot be distinguished using simple chemical tracers with multiple emission sources. Although OPE does not statistically vary with either wind direction or chemical tracer analyses, the similarity provides a point of comparison between the observations and box model simulations described below.

### 3.4. Box Model Simulations: Maximum Photochemical $O_3$

Model simulations were constrained to SONNE diel average observations as described in section 2.4.1. With the dilution rate constant derived from a fit to 10 secondary species, the Case 1 VOC scenario simulates maximum  $O_3$  to within  $-2.5\%$  ( $-1.7\text{ ppbv}$ ) of the SONNE diel average. The average relative deviation between the model output and observations for  $O_3$  is  $-2.6\%$  (11 A.M. to 3 P.M. MDT,  $\pm 2\text{ h}$  from solar noon). Figure 8 illustrates the observed diel average and model output for  $O_3$ , which suggests an accurate base case simulation of maximum  $O_3$  produced at BAO. Deviation between simulated and observed  $O_3$  profiles after 4 P.M. MDT is the result of the constant dilution/background- $O_3$  entrainment rate that is applied to the entire 24 h simulation, as described in section S3.3.

#### 3.4.1. $NO_x$ Sensitivity

Case 1 simulations were run while constrained to SONNE observed mixing ratios of VOCs,  $NO_x$ , and temperature (as described in section 2.4). To test the sensitivity of maximum photochemical  $O_3$  to  $NO_x$ , 11 simulations were run with the Case 1 VOC scenario, scaling observed  $NO_x$  mixing ratios (displayed in Figure 2) by a factor of 0 to 5. As shown in Figure 9 and Table S6, observed SONNE  $NO_x$  mixing ratios ( $NO_x$  scaling factor = 1) produce a maximum of 16.7 ppbv of photochemical  $O_3$ , while doubling observed  $NO_x$  increases photochemical

Summer 2014 in the NFR was unseasonably cool with high thunderstorm activity (Figure S5), which can enhance the downwind transport of  $O_3$  but also inhibit the stagnation and accumulation of pollution that contributes to OH radical generation and efficient  $O_3$  production. These environmental conditions can lead to periods of time with moderate photochemical activity and  $O_3$  production of only a few ppbv, similar to the variability observed in 2014 background  $O_3$  ( $O_x$  background:  $56.7 \pm 9.3\text{ ppbv}$  ( $2\sigma$ )). Mixing and/or sampling of these

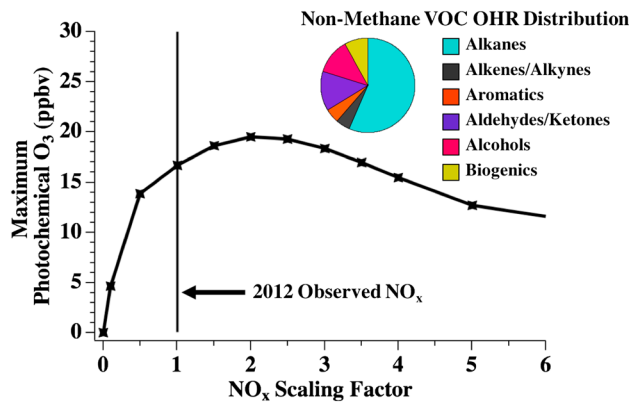


**Figure 9.** NO<sub>x</sub> sensitivity of maximum photochemical O<sub>3</sub> in the base case (Case 1) simulation. Eleven simulations are shown with SONNE (2012) observed NO<sub>x</sub> mixing ratios, represented by a scaling factor of 1, scaled from 0 to 5. The pie chart insert represents the 24 h average fractional contribution of non-methane VOCs to OH reactivity.

O<sub>3</sub> to 19.5 ppbv. Here photochemical O<sub>3</sub> is defined as the difference between simulated O<sub>3</sub> and the simultaneous mixing ratio of O<sub>3</sub> in the zero-NO<sub>x</sub> simulation. Photochemical O<sub>3</sub> production does not occur without NO<sub>x</sub>; however, O<sub>3</sub> is introduced to the model to simulate entrainment of background O<sub>3</sub> into the boundary layer (see section S3.3). O<sub>3</sub> entrainment occurs at the same rate in each simulation and is therefore represented by the zero-NO<sub>x</sub> simulation. Subtracting these mixing ratios from each nonzero-NO<sub>x</sub> simulation provides the photochemically produced O<sub>3</sub> for the given amount of NO<sub>x</sub>.

Figure 9 suggests that photochemical O<sub>3</sub> production in the region surrounding BAO is NO<sub>x</sub> limited. An increase or decrease in NO<sub>x</sub> by a factor of 2 leads to a 16.8% (±2.8 ppbv) change in maximum photochemical O<sub>3</sub>. However, NO<sub>x</sub> increases above a factor of 2 move O<sub>3</sub> production into the NO<sub>x</sub> saturated (VOC sensitive) photochemical regime, such that further increases will reduce maximum O<sub>3</sub>. These results are consistent with NO<sub>x</sub> sensitivities derived from previous 3-D modeling of NFR O<sub>3</sub> with a 2010 emission scenario [Colorado Department of Public Health and Environment (CDPHE), 2008].

**3.4.2. O&NG Influence**

To determine the average influence of O&NG emissions on maximum photochemical O<sub>3</sub>, the fraction of VOCs attributed to primary O&NG emissions was removed (Case 2) and doubled (Case 3) as described in section 2.4.2. Twenty-two additional simulations were run with these two VOC scenarios while scaling SONNE observed NO<sub>x</sub> mixing ratios between 0 and 5. Results of these simulations in comparison to Case 1 from Figure 9 are listed in Table S6 and shown in Figure 10. The pie chart inserts represent the 24 h average, non-methane VOC-class fractional contribution to VOC OHR and carbon mixing ratio (ppbC) for each VOC scenario. At observed NO<sub>x</sub> mixing ratios, the difference in maximum photochemical O<sub>3</sub> between Cases 1 and 2 (no O&NG VOC emission contribution) is 17.4%, or a 2.9 ppbv decrease. Similar to maximum O<sub>3</sub>, the O&NG VOC influence

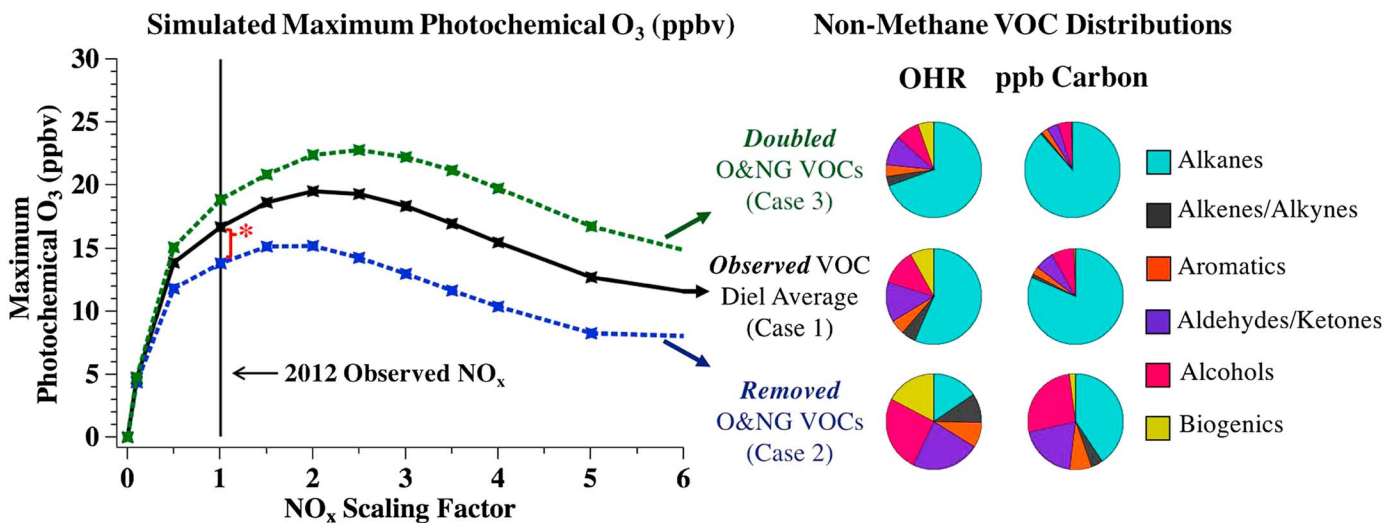


**Figure 10.** NO<sub>x</sub> sensitivity of simulated maximum photochemical O<sub>3</sub> mixing ratios for three VOC scenarios. The asterisk indicates a difference of 17.4% between observed VOC base case (Case 1) and VOC scenario with O&NG VOCs removed (Case 2) at SONNE (2012) observed NO<sub>x</sub> mixing ratios. The pie chart inserts illustrate the 24 h average non-methane VOC OHR (s<sup>-1</sup>) and carbon mixing ratio (ppbC) of each VOC scenario. Distributions do not include CH<sub>4</sub>, CO, or HCHO.

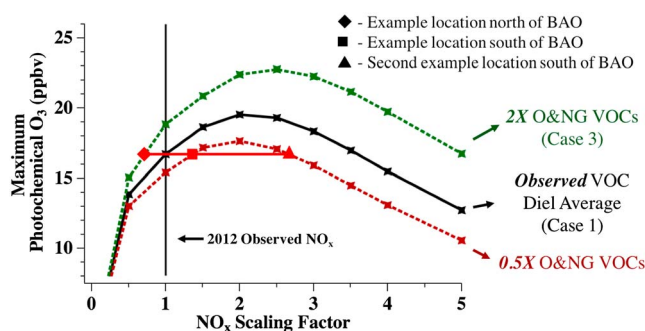


**Figure 11.**  $\text{NO}_x$  sensitivity curves for three VOC scenarios. In contrast to Figure 10, the third VOC scenario has O&NG VOCs reduced by half instead of completely removed. The red line and symbols provide example locations to the north and south of BAO with different O&NG and  $\text{NO}_x$  mixing ratios that experience the same photochemical  $\text{O}_3$  enhancement as that at BAO.

The 16.7 ppbv of photochemical  $\text{O}_3$  produced in Case 1 represents the maximum  $\text{O}_3$  enhancement under average conditions. However, 2014 observed  $\text{O}_3$  mixing ratios (Figures 5 and S1) show that  $\text{O}_3$  enhancements above background can be approximately 30 ppbv on days with high photochemical activity (e.g., high  $\text{O}_3$  and  $\text{NO}_2$  mixing ratios). As described below in section 3.4.4 and section S7, model sensitivity studies show that photochemical  $\text{O}_3$  is highly sensitive to photolysis rates, potentially explaining the large enhancements on days with photolysis rates larger than average values. In contrast, the O&NG VOC contribution to  $\text{O}_3$  (~20%) is not highly sensitive to photolysis rates (section 3.4.4). Therefore, assuming mixing ratios of VOCs and  $\text{NO}_x$  similar to their observed diel average values, the absolute contribution from O&NG VOCs could be ~6 ppbv on photochemically active days with ~30 ppbv of regional photochemical  $\text{O}_3$  production.

The total contribution of O&NG activity to photochemical  $\text{O}_3$  will depend on emissions of  $\text{NO}_x$  as well as VOCs. The difference of 17.4% highlighted in Figure 10 assumes no change in  $\text{NO}_x$  from observed mixing ratios. Applying  $\text{NO}_x$  reductions of 5.5% based on EPA NEI-2011 inventories (see section 2.4.2), Cases 1 and 2 suggest that O&NG activity contributes 18.6% (3.1 ppbv) to maximum photochemical  $\text{O}_3$ , in comparison to 17.4% (2.9 ppbv) from VOC emissions alone. However, NEI inventory estimates of O&NG  $\text{NO}_x$  emissions may be overestimated [e.g., *Ahmadov et al.*, 2015]. Thus, the total O&NG contribution to modeled maximum photochemical  $\text{O}_3$  at diel average mixing ratios of  $\text{NO}_x$  and VOCs is between 17.4 and 18.6% or 2.9 and 3.1 ppbv.

As shown in Figure 10, alkanes contributed 82% to the average SONNE non-methane carbon mixing ratio measured at BAO (Figure 10, pie chart), of which 86% are attributed to O&NG emissions (Figure 3). Despite this dominant fraction, the alkane contribution to average non-methane VOC OHR was 56% and less than 18% to maximum photochemical  $\text{O}_3$ . This result is consistent with previous literature showing that alkanes are not efficient at producing  $\text{O}_3$  [e.g., *Russell et al.*, 1995] and demonstrates the difficulty in using either carbon mixing ratio or VOC OHR for attribution of photochemically produced  $\text{O}_3$  to O&NG VOC emissions.

Despite evidence for reasonably well-mixed urban and O&NG emissions, Figure 1 suggests spatial heterogeneity in emissions from these sources, which can result in different photochemical regimes for  $\text{O}_3$  production. For example,  $\text{NO}_x$  and urban VOCs are expected in larger concentrations ~30 km south of BAO near urban-Denver [Brown et al., 2013; Swarthout et al., 2013], while O&NG VOCs may be larger ~50 km north of BAO centered in the Wattenberg Gas Field near Greeley [Swarthout et al., 2013]. However,  $\text{O}_3$  levels in exceedance of NAAQS occur across these same distances [Colorado Department of Public Health and Environment (CDPHE), 2015], suggesting a level of regional similarity in  $\text{O}_3$  enhancements. Buffering effects in the VOC- $\text{NO}_x$  sensitivity curves (Figure 11) can explain regional  $\text{O}_3$  enhancements despite different photochemical regimes. Figure 11 shows that if, for example, the absolute mixing ratios of non-O&NG VOCs remained the same but O&NG VOCs were doubled and  $\text{NO}_x$  reduced by 30% (Figure 11, red diamond), the model predicts the same maximum  $\text{O}_3$  produced as that at BAO. This implies that north of BAO, with a potentially larger abundance of O&NG VOCs, this region would be more sensitive to  $\text{NO}_x$  emission reductions. In contrast, if the non-O&NG VOCs remained the same but O&NG VOCs were reduced by 50% at two southern locations, the model predicts nearly the same maximum  $\text{O}_3$  produced for  $\text{NO}_x$  emissions 1.3 to 2.7 $\times$  higher than those at BAO

on photochemical MDA8 (maximum daily 8 h average) is a decrease of 18.4% or 2.5 ppbv. Doubling the mixing ratio of O&NG VOCs increases simulated maximum photochemical  $\text{O}_3$  by 13.2% or 2.2 ppbv, indicating a nonlinear change in  $\text{O}_3$  with O&NG VOCs. These three VOC scenarios suggest that while  $\text{O}_3$  production is sensitive to  $\text{NO}_x$  maximum and MDA8  $\text{O}_3$  mixing ratios will also respond to reductions in O&NG VOCs, again consistent with previous 3-D model results [Colorado Department of Public Health and Environment (CDPHE), 2008].

**Table 1.** Box Model Sensitivity Study Results<sup>a</sup>

Parameter	Base Case Value	Value Adjustment	Δ Max Photochemical O <sub>3</sub>		Δ OPE (%) <sup>b</sup>
			(ppbv)	(%) <sup>b</sup>	
Photolysis rates	8 A.M. MDT values: $j(\text{NO}_2) = 3.6 \times 10^{-3} \text{ s}^{-1}$ $j(\text{O}^1\text{D}) = 4.0 \times 10^{-6} \text{ s}^{-1}$	±25%	+6.0/−5.4	+35.9/−32.3	+4.6/−3.1
Dilution	$k = 1.05 \times 10^{-4} \text{ s}^{-1}$	±10%	±2.3	±13.8	±1.5
Temperature	SONNE observations	±10%	+1.3/−1.1	+7.8/−7.1	-
Background O <sub>3</sub>	58 ppbv	±10%	±0.8	±4.8	+7.7/−6.2
Enhanced CH <sub>4</sub>	SONNE observations-background	±10%	±0.1	±0.6	±3.1
O <sub>3</sub> deposition	$k = 3.5 \times 10^{-6} \text{ s}^{-1}$	±10%	±<0.1	-	-
Albedo	0.067	±10%	±<0.1	-	-
HNO <sub>3</sub> deposition	$k = 2.2 \times 10^{-5} \text{ s}^{-1}$	−100%	−<0.1	-	+7.7 <sup>c</sup>

<sup>a</sup>Calculated for Case 1 VOC scenario at NO<sub>x</sub> scaling factor = 1.

<sup>b</sup>Values not provided if change is <0.1 ppbv (max photochemical O<sub>3</sub>) or <0.1 ppbv/ppbv (OPE).

<sup>c</sup>HNO<sub>3</sub> deposition artificially increases modeled OPE by 7.7%; all OPE simulations were run without HNO<sub>3</sub> deposition as this does not change photochemical O<sub>3</sub> and is necessary to accurately model OPE.

(Figure 11, red box and triangle). O<sub>3</sub> production at the second of these points (red triangle) is in the NO<sub>x</sub>-saturated regime but still produces the same photochemical O<sub>3</sub> as at the NO<sub>x</sub>-limited BAO. These scenarios suggest that O<sub>3</sub> enhancements in the NFR can be regional, while effective control strategies should still be informed by finer scale VOC/NO<sub>x</sub> observations.

### 3.4.3. Model Ozone Production Efficiency

Case 1 and 2 simulations, as described above, were used to calculate the influence of O&NG VOC emissions on modeled OPEs. The OPE of each model simulation was calculated from the average ΔO<sub>x</sub>/ΔNO<sub>z</sub> ratio between 11 A.M. to 3 P.M. MDT, the same time period during which the model was fit to best reproduce 10 secondary products (see section S3.3). Here ΔO<sub>x</sub> and ΔNO<sub>z</sub> are used to capture photochemical O<sub>3</sub> production and NO<sub>x</sub> oxidation. Delta O<sub>x</sub> and ΔNO<sub>z</sub> are defined as the difference between the O<sub>x</sub> and NO<sub>z</sub> mixing ratios in a given simulation and the simultaneous values in the zero-NO<sub>x</sub> simulation (as described in section 3.4.1). The HNO<sub>3</sub> dilution rate constant was the same as all other 4001 species ( $k = 1.05 \times 10^{-4} \text{ s}^{-1}$ ), but its deposition rate was set to  $0 \text{ s}^{-1}$  to remove the influence of HNO<sub>3</sub> loss on NO<sub>z</sub>. Eliminating HNO<sub>3</sub> deposition does not impact simulated maximum photochemical O<sub>3</sub> but does increase Case 1 OPE by 7.7% (see Table 1). Simulated OPE was also found to decrease with increasing NO<sub>x</sub> mixing ratios, consistent with previous OPE model simulation results [e.g., Lin et al., 1988].

At a NO<sub>x</sub> scaling factor of 1, OPEs derived from the Case 1 and 2 VOC scenarios are 6.5 ppbv/ppbv (±0.5) and 5.2 ppbv/ppbv (±0.5), respectively. The errors are derived from the quadrature addition of OPE uncertainties associated with model parameters listed in Table 1 (not including HNO<sub>3</sub> deposition). These results suggest that O&NG VOC emissions increase the efficiency of O<sub>3</sub> production at BAO by 1.3 ppbv/ppbv (20%). To account for NEI-estimated O&NG NO<sub>x</sub> emissions (see section 2.4.2), the OPE for Case 2 (no O&NG VOCs) was calculated at a NO<sub>x</sub> scaling factor of 0.945 (−5.5%). The OPE influence of O&NG emissions did not change, as this small NO<sub>x</sub> reduction did not influence the simulated OPE by >0.1 ppbv/ppbv. The similarity between Cases 1 and 2 suggests that the OPE influence of O&NG emissions is small enough to be obscured in observations at BAO due to air transport and mixing, as discussed previously in section 3.3.1.1.

### 3.4.4. Model Sensitivity Studies

As described above, simulations for all three VOC scenarios were constrained every 30 min to chemical species and physical parameters. The only tunable model parameter was the dilution rate constant, which was derived by minimizing the deviation between observations and model output for 10 select secondary products, including O<sub>3</sub>. A ±10% change in the dilution rate constant changes simulated maximum photochemical O<sub>3</sub> in Case 1 by +1.3/−1.1 ppbv (+7.8/−6.6%) and average model-to-observation relative deviation of all 10 compounds by +1.6/−1.2%.

Case 1 (at observed NO<sub>x</sub> mixing ratios) was additionally tested for sensitivities to ±10% changes in other model constraints including photolysis rates, albedo, temperature, background O<sub>3</sub>, enhanced CH<sub>4</sub>, and O<sub>3</sub>/HNO<sub>3</sub>

deposition rates (see Table 1). Sensitivity differences between maximum photochemical  $O_3$  and OPE can be explained by the additional dependence of OPE on photochemical  $NO_x$  oxidation. Of the parameters tested, OPE is most sensitive to changes in temperature, while maximum photochemical  $O_3$  is most sensitive to changes in photolysis rates (more than the dilution rate constant) and increases by as much as 13.8% with a 10% increase in both  $j(NO_2)$  and  $j(O^1D)$  scaling factors. Observations of  $j(NO_2)$  and  $j(O^1D)$  are not known with greater than 25% accuracy, which will change absolute maximum photochemical  $O_3$  by  $+6.0/-5.4$  ppbv ( $+35.9/-32.3\%$ ). To test the sensitivity of the main box model results to photolysis rates, 15 additional simulations were run for Cases 1 and 2, while scaling photolysis rates by  $\pm 25\%$ . The difference in maximum photochemical  $O_3$  between Cases 1 and 2 is not as sensitive to changes in photolysis as is the absolute maximum simulated  $O_3$  (Figures S10 and S11). In other words, regardless of 25% changes in photolysis rates, BAO photochemical  $O_3$  remains sensitive to  $NO_x$  (Figure S10) and the O&NG VOC influence ranges from 15.1 to 19.4% (Figure S11), within 2.3% of 17.4% derived under original photolysis conditions.

#### 4. Conclusions

The Northern Front Range of Colorado has been in nonattainment with the NAAQS for  $O_3$  since 2007. Summertime photochemical  $O_3$  in the NFR is influenced by regional  $NO_x$  emissions, concentrated around urban-Denver, and large VOC emissions from a rapidly developing O&NG basin. The BAO site lies between these major regional emission sectors and exhibits influence from each (O&NG, urban, and agriculture). Data from this site were used to quantify the influence of O&NG emissions on  $O_3$  production using an observationally constrained box model and metrics of VOC OHR and OPE.

OPEs derived from 2014  $O_x/NO_2$  correlations at 15 min time intervals during 27 afternoons have an average of  $2.9 \pm 4.4$  ppbv/ppbv ( $1\sigma$ ) for all determinations and  $5.3 \pm 3.6$  ppbv/ppbv ( $-2.0/+0.6$ ) for a smaller subset with high correlation between  $O_x$  and  $NO_2$ . A difference in average OPE could not be statistically distinguished for air primarily influenced by O&NG and urban emissions using observed wind direction, modeled back-trajectories, or simple chemical tracers. These results suggest that the OPE influence of O&NG and urban emissions at BAO is obscured by air mixing and/or do not differ to within 1.8 ppbv/ppbv. The simulated OPE difference of 1.3 ppbv/ppbv with and without O&NG primary VOCs falls within the uncertainty of the 2014 observational analyses.

Box model simulations constrained to diel average chemical and physical observations indicate that maximum photochemical  $O_3$  at BAO is  $NO_x$  sensitive. Simulations with removed and doubled primary O&NG VOC contributions showed that O&NG VOC emissions contribute on average 17.4% (2.9 ppbv) to maximum photochemical  $O_3$  and scale nonlinearly with changes in O&NG VOCs. NEI emissions of O&NG  $NO_x$  are estimated to contribute up to an additional 1.2% (0.20 ppbv) to the total contribution of O&NG activity to maximum  $O_3$  photochemically produced at BAO. Alkanes contributed on average 82% to the observed carbon mixing ratio, of which 86% could be attributed to O&NG emissions. However, alkanes only contributed 56% to VOC OHR and less than 18% to modeled maximum photochemical  $O_3$ .

Future work in the NFR is required to address several key uncertainties. First, detailed multiyear studies are required to assess the influence of rapid changes in O&NG and urban activities on ambient levels of VOCs and  $NO_x$  and the sensitivity of photochemical  $O_3$  production. Between 2012 and 2014, the number of active wells in Weld County increased by  $\sim 2000$ , oil production more than doubled, and natural gas production increased by a factor of  $\sim 1.6$  [Colorado Oil and Gas Conservation Commission (COGCC), 2/2016]. Since early 2015, O&NG drilling activity has declined nationwide. In addition, the NFR population has increased by 12% to over 3 million people since 2010 [United States Department of Agriculture (USDA), 2016] and continues to grow, influencing the absolute emissions of  $NO_x$  and distribution across the region. Such rapid changes in O&NG activity and urban development suggest the potential for year-to-year changes in photochemical  $O_3$  sensitivities and emissions of VOC and  $NO_x$ .

Second, spatially distributed studies from across the region are required to understand the differences in  $O_3$  sensitivities in the more VOC impacted areas to the north and  $NO_x$  impacted areas to the south. Analysis of recent 2014 and 2015 field studies should be informative. Future studies incorporating the type of detailed measurements and models presented here at ground sites that span the NFR would serve to improve the

understanding of regional O<sub>3</sub> production sensitivities to VOCs and NO<sub>x</sub>, as well address recent trends in emissions of both urban and O&NG NO<sub>x</sub> and VOCs.

### List of Primary Acronyms

BAO –Boulder Atmospheric Observatory  
 CRD –Cavity Ring Down  
 DISCOVER-AQ –Deriving Information on Surface Conditions from Column and Vertically Resolved Observations Relevant to Air Quality  
 DSMACC –Dynamically Simple Model of Atmospheric Chemical Complexity  
 EPA –Environmental Protection Agency  
 FRAPPÉ –Front Range Air Pollution and Photochemistry Experiment  
 MCM –Master Chemical Mechanism  
 MDA8 –Maximum Daily 8-h Average  
 MDT –Mountain Daylight Time  
 NAAQS –National Ambient Air Quality Standard  
 NEI –National Emission Inventory  
 NFR –Northern Front Range  
 O&NG –Oil and Natural Gas  
 OHR –VOC OH Reactivity  
 OPE –Ozone Production Efficiency  
 ppbC –parts per billion of Carbon  
 SONNE –Summer Ozone Near Natural gas Emissions  
 TUV –Tropospheric Ultraviolet and Visible radiation model  
 VOC –Volatile Organic Compound

### Acknowledgments

This work was supported by NOAA's Atmospheric Chemistry, Carbon Cycle, and Climate Program. We thank Rebecca S. Hornbrook, Eric C. Apel, and Alan J. Hills for TOGA data from FRAPPÉ 2014 and comments during the manuscript preparation process. We thank Betsy Weatherhead for her contribution to the statistical analysis. We also thank Patrick Reddy for insightful comments and discussion during preparation and Frank Flocke and Gabriele Pfister for FRAPPÉ campaign organization. Emily V. Fischer acknowledges support from the Colorado Department of Public Health and the Environment (CDPHE). Meteorological data from the Boulder Atmospheric Observatory (2012 and 2014) are available at <http://www.esrl.noaa.gov/psd/technology/bao/> and <http://www.esrl.noaa.gov/gmd/dv/data/?category=Ozone&site=BAO>, SONNE data available at <http://esrl.noaa.gov/csd>, FRAPPÉ data are available at <http://www-air.larc.nasa.gov>, NASA OMI total O<sub>3</sub> column available at <http://mirador.gsfc.nasa.gov>, and CalNEX CO and VOCs are available at <http://esrl.noaa.gov/csd>. All referenced supplemental text, figures, and tables can be found in the supporting information.

### References

- Ahmadov, R., et al. (2015), Understanding high wintertime ozone pollution events in an oil- and natural gas-producing region of the western US, *Atmos. Chem. Phys.*, *15*(1), 411–429, doi:10.5194/acp-15-411-2015.
- Alvarez, R. J., et al. (2011), Development and application of a compact, tunable, solid-state airborne ozone lidar system for boundary layer profiling, *J. Atmos. Oceanic Technol.*, *28*(10), 1258–1272, doi:10.1175/Jtech-D-10-05044.1.
- Augustine, J. A., J. J. DeLuisi, and C. N. Long (2000), SURFRAD—A national Surface Radiation Budget Network for atmospheric research, *Bull. Am. Meteorol. Soc.*, *81*(10), 2341–2357, doi:10.1175/1520-0477(2000)081<2341:SANSRB>2.3.CO;2.
- Brantley, H. L., E. D. Thoma, and A. P. Eisele (2015), Assessment of volatile organic compound and hazardous air pollutant emissions from oil and natural gas well pads using mobile remote and on-site direct measurements, *J. Air Waste Manage.*, *65*(9), 1072–1082, doi:10.1080/10962247.2015.1056888.
- Brown, S. S., et al. (2013), Nitrogen, Aerosol Composition, and Halogens on a Tall Tower (NACHTT): Overview of a wintertime air chemistry field study in the front range urban corridor of Colorado, *J. Geophys. Res. Atmos.*, *118*, 8067–8085, doi:10.1002/jgrd.50537.
- Butler, T. J., F. M. Vermeylen, M. Rury, G. E. Likens, B. Lee, G. E. Bowker, and L. McCluney (2011), Response of ozone and nitrate to stationary source NO<sub>x</sub> emission reductions in the eastern USA, *Atmos. Environ.*, *45*(5), 1084–1094, doi:10.1016/j.atmosenv.2010.11.040.
- Carlton, A. G., E. Little, M. Moeller, S. Odoyo, and P. B. Shepson (2014), The data gap: Can a lack of monitors obscure loss of Clean Air Act benefits in fracking areas? *Environ. Sci. Technol.*, *48*(2), 893–894, doi:10.1021/es405672t.
- Carter, W. P. L., and J. H. Seinfeld (2012), Winter ozone formation and VOC incremental reactivities in the Upper Green River Basin of Wyoming, *Atmos. Environ.*, *50*, 255–266, doi:10.1016/j.atmosenv.2011.12.025.
- Chameides, W. L. (1978), The photochemical role of tropospheric nitrogen oxides, *Geophys. Res. Lett.*, *5*(1), 17–20, doi:10.1029/GL005i001p00017.
- Chen, H., et al. (2010), High-accuracy continuous airborne measurements of greenhouse gases (CO<sub>2</sub> and CH<sub>4</sub>) using the cavity ring-down spectroscopy (CRDS) technique, *Atmos. Meas. Tech.*, *3*(2), 375–386, doi:10.5194/amt-3-375-2010.
- Chen, H., A. Karion, C. W. Rella, J. Winderlich, C. Gerbig, A. Filges, T. Newberger, C. Sweeney, and P. P. Tans (2013), Accurate measurements of carbon monoxide in humid air using the cavity ring-down spectroscopy (CRDS) technique, *Atmos. Meas. Tech.*, *6*(4), 1031–1040, doi:10.5194/amt-6-1031-2013.
- Colorado Department of Public Health and Environment (CDPHE) (2008), Denver metro area & north front range 8-hour ozone State Implementation Plan (SIP) Technical Support Documents (TSD), Appendix E, Executive Summary. [Available at <http://www.colorado.gov/airquality/documents/deno308/>]
- Colorado Department of Public Health and Environment (CDPHE) (2015), Ozone standard exceedance summary table. [Available at [http://www.colorado.gov/airquality/html\\_resources/ozone\\_summary\\_table.pdf](http://www.colorado.gov/airquality/html_resources/ozone_summary_table.pdf)]. Colorado.gov.
- Colorado Department of Public Health and Environment (CDPHE) (2016), Ozone information. [Available at <https://www.colorado.gov/pacific/cdphe/ozone-information>].
- Colorado Oil and Gas Conservation Commission (COGCC) (1/2016), Oil and natural gas wells data available in the “Downloads” section. [Available at <http://cogcc.state.co.us/data2.html/-/downloads>].
- Colorado Oil and Gas Conservation Commission (COGCC) (2/2016), County level production available in the “DataBase” section. [Available at <http://cogcc.state.co.us/>]

- Cooper, O. R., R.-S. Gao, D. Tarasick, T. Leblanc, and C. Sweeney (2012), Long-term ozone trends at rural ozone monitoring sites across the United States, 1990–2010, *J. Geophys. Res.*, *117*, D22307, doi:10.1029/2012JD018261.
- Cooper, O. R., A. O. Langford, D. D. Parrish, and D. W. Fahey (2015), Challenges of a lowered U.S. ozone standard, *Science*, *348*(6239), 1096–1097.
- Crook, N. A., T. L. Clark, and M. W. Moncrieff (1990), The Denver Cyclone. Part I: Generation in low Froude number flow, *J. Atmos. Sci.*, *47*(23), 2725–2742, doi:10.1175/1520-0469(1990)047<2725:TDCPIG>2.0.CO;2.
- Crosson, E. R. (2008), A cavity ring-down analyzer for measuring atmospheric levels of methane, carbon dioxide, and water vapor, *Appl. Phys. B*, *92*(3), 403–408, doi:10.1007/s00340-008-3135-y.
- Crutzen, P. J. (1970), The influence of nitrogen oxides on the atmospheric ozone content, *Q. J. R. Meteorol. Soc.*, *96*(408), 320–325, doi:10.1002/qj.49709640815.
- Duncan, B. N., L. N. Lamsal, A. M. Thompson, Y. Yoshida, Z. Lu, D. G. Streets, M. M. Hurwitz, and K. E. Pickering (2016), A space-based, high-resolution view of notable changes in urban NO<sub>x</sub> pollution around the world (2005–2014), *J. Geophys. Res. Atmos.*, *121*, 976–996, doi:10.1002/2015JD024121.
- Edwards, P. M., et al. (2013), Ozone photochemistry in an oil and natural gas extraction region during winter: simulations of a snow-free season in the Uintah Basin, Utah, *Atmos. Chem. Phys.*, *13*(17), 8955–8971, doi:10.5194/acp-13-8955-2013.
- Edwards, P. M., et al. (2014), High winter ozone pollution from carbonyl photolysis in an oil and gas basin, *Nature*, *514*(7522), 351–354, doi:10.1038/nature13767.
- Emmerson, K. M., and M. J. Evans (2009), Comparison of tropospheric gas-phase chemistry schemes for use within global models, *Atmos. Chem. Phys.*, *9*(5), 1831–1845, doi:10.5194/acp-9-1831-2009.
- Environmental Protection Agency (US EPA) (2016), National Emissions Inventory (NEI) air pollutant emissions trends data. [Available at <https://www.epa.gov/air-emissions-inventories/air-pollutant-emissions-trends-data>.]
- Field, R. A., J. Soltis, M. C. McCarthy, S. Murphy, and D. C. Montague (2015), Influence of oil and gas field operations on spatial and temporal distributions of atmospheric non-methane hydrocarbons and their effect on ozone formation in winter, *Atmos. Chem. Phys.*, *15*(6), 3527–3542, doi:10.5194/acp-15-3527-2015.
- Fuchs, H., W. P. Dube, B. M. Lerner, N. L. Wagner, E. J. Williams, and S. S. Brown (2009), A sensitive and versatile detector for atmospheric NO<sub>2</sub> and NO<sub>x</sub> based on blue diode laser cavity ring-down spectroscopy, *Environ. Sci. Technol.*, *43*(20), 7831–7836, doi:10.1021/es902067h.
- Gentner, D. R., et al. (2014), Emissions of organic carbon and methane from petroleum and dairy operations in California's San Joaquin Valley, *Atmos. Chem. Phys.*, *14*(10), 4955–4978, doi:10.5194/acp-14-4955-2014.
- Gerbig, C., S. Schmitgen, D. Kley, A. Volz-Thomas, K. Dewey, and D. Haaks (1999), An improved fast-response vacuum-UV resonance fluorescence CO instrument, *J. Geophys. Res.*, *104*(D1), 1699–1704, doi:10.1029/1998JD100031.
- Gilman, J. B., J. F. Burkhart, B. M. Lerner, E. J. Williams, and W. C. Kuster (2010), Ozone variability and halogen oxidation within the Arctic and sub-Arctic springtime boundary layer, *Atmos. Chem. Phys.*, *10*(21), 10,223–10,236.
- Gilman, J. B., B. M. Lerner, W. C. Kuster, and J. A. de Gouw (2013), Source signature of volatile organic compounds from oil and natural gas operations in northeastern Colorado, *Environ. Sci. Technol.*, *47*(3), 1297–1305, doi:10.1021/es304119a.
- Griffin, R. J., C. A. Johnson, R. W. Talbot, H. Mao, R. S. Russo, Y. Zhou, and B. C. Sive (2004), Quantification of ozone formation metrics at Thompson Farm during the New England Air Quality Study (NEAQS) 2002, *J. Geophys. Res.*, *109*, D24302, doi:10.1029/2004JD005344.
- Harrison, L. L., J. Michalsky, and J. Berndt (1994), Automated multifilter rotating shadow-band radiometer: An instrument for optical depth and radiation measurements, *Appl. Opt.*, *33*(22), 5118–5125.
- Helmig, D., C. R. Thompson, J. Evans, P. Boylan, J. Hueber, and J. H. Park (2014), Highly elevated atmospheric levels of volatile organic compounds in the Uintah Basin, Utah, *Environ. Sci. Technol.*, *48*(9), 4707–4715, doi:10.1021/es405046r.
- Hirsch, A. I., J. W. Munger, D. J. Jacob, L. W. Horowitz, and A. H. Goldstein (1996), Seasonal variation of the ozone production efficiency per unit NO<sub>x</sub> at Harvard Forest, Massachusetts, *J. Geophys. Res.*, *101*(D7), 12,659–12,666, doi:10.1029/96JD00557.
- Jenkin, M. E., J. C. Young, and A. R. Rickard (2015), The MCM v3.3.1 degradation scheme for isoprene, *Atmos. Chem. Phys.*, *15*(20), 11,433–11,459, doi:10.5194/acp-15-11433-2015.
- Kaimal, J. C., and J. E. Gaynor (1983), The Boulder Atmospheric Observatory, *J. Climate Appl. Meteorol.*, *22*(5), 863–880.
- Kemball-Cook, S., A. Bar-Ilan, J. Grant, L. Parker, J. Jung, W. Santamaria, J. Mathews, and G. Yarwood (2010), Ozone impacts of natural gas development in the Haynesville Shale, *Environ. Sci. Technol.*, *44*(24), 9357–9363, doi:10.1021/es1021137.
- Kleinman, L., P. H. Daum, Y.-N. Lee, L. J. Nunnermacker, S. R. Springston, J. Weinstein-Lloyd, and J. Rudolph (2002), Ozone production efficiency in an urban area, *J. Geophys. Res.*, *107*(D23), 4733, doi:10.1029/2002JD002529.
- Langford, A. O., et al. (2015), An overview of the 2013 Las Vegas Ozone Study (LVOS): Impact of stratospheric intrusions and long-range transport on surface air quality, *Atmos. Environ.*, *109*, 305–322, doi:10.1016/j.atmosenv.2014.08.040.
- Lin, X., M. Trainer, and S. C. Liu (1988), On the nonlinearity of the tropospheric ozone production, *J. Geophys. Res.*, *93*(D12), 15,879–15,888, doi:10.1029/JD093iD12p15879.
- Madronich, S. S., R. L. McKenzie, L. O. Bjorn, and M. M. Caldwell (1998), Changes in biologically active ultraviolet radiation reaching the Earth's surface, *J. Photochem. Photobiol.*, *B*, *46*(1–3), 5–19.
- McManus, J. B., J. H. Shorter, D. D. Nelson, M. S. Zahniser, D. E. Glenn, and R. M. McGovern (2008), Pulsed quantum cascade laser instrument with compact design for rapid, high sensitivity measurements of trace gases in air, *Appl. Phys. B*, *92*(3), 387–392, doi:10.1007/s00340-008-3129-9.
- Michalsky, J. J., and G. B. Hodges (2013), Field measured spectral albedo—Four years of data from the Western U.S. Prairie, *J. Geophys. Res. Atmos.*, *118*, 813–825, doi:10.1002/jgrd.50149.
- Neuman, J. A., et al. (2009), Relationship between photochemical ozone production and NO<sub>x</sub> oxidation in Houston, Texas, *J. Geophys. Res.*, *114*, D00F08, doi:10.1029/2008JD011688.
- Nunnermacker, L. J., et al. (1998), Characterization of the Nashville urban plume on July 3 and July 18, 1995, *J. Geophys. Res.*, *103*(D21), 28,129–28,148, doi:10.1029/98JD01961.
- Olszyna, K. J., E. M. Bailey, R. Simonaitis, and J. F. Meagher (1994), O<sub>3</sub> and NO<sub>y</sub> relationships at a rural site, *J. Geophys. Res.*, *99*(D7), 14,557–14,563, doi:10.1029/94JD00739.
- Oltmans, S., R. Schnell, B. Johnson, G. Petron, T. Mefford, and R. Neely (2014), Anatomy of wintertime ozone associated with oil and natural gas extraction activity in Wyoming and Utah, *Elementa Sci. Anthropocene*, *2*, 000024, doi:10.12952/journal.elementa.000024.
- Pacsi, A. P., Y. Kimura, G. McGaughey, E. C. McDonald-Buller, and D. T. Allen (2015), Regional ozone impacts of increased natural gas use in the Texas power sector and development in the Eagle Ford Shale, *Environ. Sci. Technol.*, *49*(6), 3966–3973, doi:10.1021/es5055012.
- Peischl, J., et al. (2012), Airborne observations of methane emissions from rice cultivation in the Sacramento Valley of California, *J. Geophys. Res.*, *117*, D00V25, doi:10.1029/2012JD017994.
- Pétron, G., et al. (2012), Hydrocarbon emissions characterization in the Colorado Front Range: A pilot study, *J. Geophys. Res.*, *117*, D04304, doi:10.1029/2011JD016360.

- Pétron, G., et al. (2014), A new look at methane and non-methane hydrocarbon emissions from oil and natural gas operations in the Colorado Denver-Julesburg Basin, *J. Geophys. Res. Atmos.*, *119*, 6836–6852, doi:10.1002/2013JD021272.
- Rappenglück, B., et al. (2014), Strong wintertime ozone events in the Upper Green River basin, Wyoming, *Atmos. Chem. Phys.*, *14*(10), 4909–4934, doi:10.5194/acp-14-4909-2014.
- Rodriguez, M. A., M. G. Barna, and T. Moore (2009), Regional impacts of oil and gas development on ozone formation in the Western United States, *J. Air Waste Manage.*, *59*(9), 1111–1118, doi:10.3155/1047-3289.59.9.1111.
- Roelofs, G.-J., and J. Lelieveld (1995), Distribution and budget of O<sub>3</sub> in the troposphere calculated with a chemistry general circulation model, *J. Geophys. Res.*, *100*(D10), 20,983–20,998, doi:10.1029/95JD02326.
- Russell, A., J. Milford, M. S. Bergin, S. McBride, L. McNair, Y. Yang, W. R. Stockwell, and B. Croes (1995), Urban ozone control and atmospheric reactivity of organic gases, *Science*, *269*(5223), 491–495, doi:10.1126/science.269.5223.491.
- Rutter, A. P., R. J. Griffin, B. K. Cevik, K. M. Shakyia, L. Gong, S. Kim, J. H. Flynn, and B. L. Lefer (2015), Sources of air pollution in a region of oil and gas exploration downwind of a large city, *Atmos. Environ.*, *120*, 89–99, doi:10.1016/j.atmosenv.2015.08.073.
- Ryerson, T. B., et al. (1998), Emissions lifetimes and ozone formation in power plant plumes, *J. Geophys. Res.*, *103*(D17), 22,569–22,583, doi:10.1029/98JD01620.
- Schnell, R. C., S. J. Oltmans, R. R. Neely, M. S. Endres, J. V. Molenar, and A. B. White (2009), Rapid photochemical production of ozone at high concentrations in a rural site during winter, *Nat. Geosci.*, *2*(2), 120–122.
- Shetter, R. E., et al. (2003), Photolysis frequency of NO<sub>2</sub>: Measurement and modeling during the International Photolysis Frequency Measurement and Modeling Intercomparison (IPMMI), *J. Geophys. Res.*, *108*(D16), 8544, doi:10.1029/2002JD002932.
- Sillman, S., D. He, M. R. Pippin, P. H. Daum, D. G. Imre, L. I. Kleinman, J. H. Lee, and J. Weinstein-Lloyd (1998), Model correlations for ozone, reactive nitrogen, and peroxides for Nashville in comparison with measurements: Implications for O<sub>3</sub>-NO<sub>x</sub>-hydrocarbon chemistry, *J. Geophys. Res.*, *103*(D17), 22,629–22,644, doi:10.1029/98JD00349.
- St. John, J. C., W. L. Chameides, and R. Saylor (1998), Role of anthropogenic NO<sub>x</sub> and VOC as ozone precursors: A case study from the SOS Nashville/Middle Tennessee Ozone Study, *J. Geophys. Res.*, *103*(D17), 22,415–22,423, doi:10.1029/98JD00973.
- Swarthout, R. F., R. S. Russo, Y. Zhou, A. H. Hart, and B. C. Sive (2013), Volatile organic compound distributions during the NACHTT campaign at the Boulder Atmospheric Observatory: Influence of urban and natural gas sources, *J. Geophys. Res. Atmos.*, *118*, 10,614–10,637, doi:10.1002/jgrd.50722.
- Swarthout, R. F., R. S. Russo, Y. Zhou, B. M. Miller, B. Mitchell, E. Horsman, E. Lipsky, D. C. McCabe, E. Baum, and B. C. Sive (2015), Impact of Marcellus Shale natural gas development in southwest Pennsylvania on volatile organic compound emissions and regional air quality, *Environ. Sci. Technol.*, *49*(5), 3175–3184, doi:10.1021/es504315f.
- Szoke, E. J. (1991), Eye of the Denver Cyclone, *Mon. Weather Rev.*, *119*(5), 1283–1292, doi:10.1175/1520-0493(1991)119<1283:EOTDC>2.0.CO;2.
- Szoke, E. J., M. L. Weisman, J. M. Brown, F. Caracena, and T. W. Schlatter (1984), A subsynoptic analysis of the Denver tornadoes of 3 June 1981, *Mon. Weather Rev.*, *112*(4), 790–808, doi:10.1175/1520-0493(1984)112<0790:ASAOTD>2.0.CO;2.
- Toth, J. J., and R. H. Johnson (1985), Summer surface flow characteristics over northeast Colorado, *Mon. Weather Rev.*, *113*(9), 1458–1469, doi:10.1175/1520-0493(1985)113<1458:SSFCON>2.0.CO;2.
- Trainer, M., et al. (1993), Correlation of ozone with NO<sub>y</sub> in photochemically aged air, *J. Geophys. Res.*, *98*(D2), 2917–2925, doi:10.1029/92JD01910.
- Trainer, M., B. A. Ridley, M. P. Buhr, G. Kok, J. Walega, G. Hübler, D. D. Parrish, and F. C. Fehsenfeld (1995), Regional ozone and urban plumes in the southeastern United States: Birmingham, A case study, *J. Geophys. Res.*, *100*(D9), 18,823–18,834, doi:10.1029/95JD01641.
- United States Department of Agriculture (USDA) (2016), 2012 census of agriculture, county level data available from the USDA National Agricultural Statistics Service Quick Stats. [Available at <http://quickstats.nass.usda.gov/>]
- Washenfelder, R. A., N. L. Wagner, W. P. Dube, and S. S. Brown (2011a), Measurement of atmospheric ozone by cavity ring-down spectroscopy, *Environ. Sci. Technol.*, *45*(7), 2938–2944, doi:10.1021/es103340u.
- Washenfelder, R. A., et al. (2011b), The glyoxal budget and its contribution to organic aerosol for Los Angeles, California, during CalNex 2010, *J. Geophys. Res.*, *116*, D00V02, doi:10.1029/2011JD016314.
- Wilczak, J. M., and J. W. Glendening (1988), Observations and mixed-layer modeling of a terrain-induced mesoscale gyre: The Denver Cyclone, *Mon. Weather Rev.*, *116*(12), 2688–2711, doi:10.1175/1520-0493(1988)116<2688:OAMLMO>2.0.CO;2.
- Wild, R. J., et al. (2014), A measurement of total reactive nitrogen, NO<sub>y</sub>, together with NO<sub>2</sub>, NO, and O<sub>3</sub> via cavity ring-down spectroscopy, *Environ. Sci. Technol.*, *48*(16), 9609–9615, doi:10.1021/es501896w.
- Zaveri, R. A., C. M. Berkowitz, L. I. Kleinman, S. R. Springston, P. V. Doskey, W. A. Lonneman, and C. W. Spicer (2003), Ozone production efficiency and NO<sub>x</sub> depletion in an urban plume: Interpretation of field observations and implications for evaluating O<sub>3</sub>-NO<sub>x</sub>-VOC sensitivity, *J. Geophys. Res.*, *108*(D14), 4436, doi:10.1029/2002JD003144.